Ore Geology Reviews 73 (2016) 313–329

Contents lists available at ScienceDirect

Ore Geology Reviews

journal homepage: www.elsevier.com/locate/oregeorev

The geology and geochemistry of Jinchangyu gold deposit, North China Craton: Implications for metallogenesis and geodynamic setting

Yang Song [a], Si-Hong Jiang [a], Leon Bagas [b], Chao Li [c], Jian-Zhong Hu [d], Qing Zhang [d], Wei Zhou [d], Hai-Yang Ding [d]

[a] MLR Key Laboratory of Metallogeny and Mineral Assessment Institute of Mineral Resources, CAGS, Beijing 100037, China
[b] Centre for Exploration Targeting, ARC Centre of Excellence for Core to Crust Fluid Systems, The University of Western Australia, Crawley, WA 6009, Australia
[c] National Research Center of Geoanalysis, Beijing 100037, China
[d] China University of Geosciences, Beijing 100083, China

ARTICLE INFO

Article history:
Received 29 April 2014
Received in revised form 21 October 2014
Accepted 26 October 2014
Available online 20 November 2014

Keywords:
Jinchangyu Au deposit
Archaean Zunhua Group
North China Craton
Late Triassic
Albite alteration

ABSTRACT

The Jinchangyu Au deposits contained an original resource of 50 t of gold and is located close to the northeastern margin of the North China Craton (NCC). The orebodies are controlled by structures in the amphibolite units of the Archaean Zunhua Group. Mineralization is generally associated with albite and hematite which is indicative of Na–Al–Si–Fe alteration. The most common styles of mineralization are subdivided based on the cross-cutting relationships of mineral assemblages as follows: (i) quartz–albite–hematite; (ii) quartz–albite–polymetallic sulfides with gold and molybdenite; (iii) quartz–pyrite; and (iv) quartz–carbonate. Quartz samples from the second (Stage II) and third (Stage III) assemblages contain two-phase fluid inclusion types; these are: (i) CO_2–H_2O fluid inclusions, and (ii) daughter mineral-bearing inclusions, which have homogenization temperatures of 270°–350 °C (for assemblage Stage II) and 180°–240 °C (for Stage III), and salinities of ≤13 wt.% NaCl equiv. A few S-type fluid inclusions suggesting salinities of 27.6–28.3 wt.% NaCl equiv. The S isotope composition of pyrite and molybdenite from Stage II ($\delta^{34}S = -4.4$ to 1.9‰) indicates that the mineralizing fluid originated predominantly from a magmatic source. The H–O isotope signatures from Stage II indicate a magmatic-dominated source for the mineralizing fluid with some addition of meteoric fluids. Previously published Pb and C isotope data indicate that ore and magma in the eastern part of the Hebei Province of China interacted with Precambrian country rocks, and so the fluids moved from the lower crust to shallower level during mineralization. The red quartz–albite–hematite veins from Jinchangyu were generated under strongly oxidizing alkaline conditions that were favorable for the incorporation of gold into the fluid and the crystallization of albite during the early stage of gold deposition.

Seven molybdenite samples from Jinchangyu yield Re–Os model ages of ca. 233 to 219 Ma with a weighted mean age of 225 ± 4 Ma and an isochron age of 223 ± 5 Ma. This indicates that at least some of the gold associated with molybdenite is Late Triassic in age, and could be associated with buried intrusions that are part of the Late Triassic Dushan granites in the eastern portion of the NCC. This mineralization was formed after the closure of the Paleo-Asian Ocean. These results indicate that the intrusion-related Jinchangyu deposit is the far-field structural product of the collision of the NCC with the Siberian Craton to the north along the northern margin of the NCC.

1. Introduction

The Eastern Hebei Province is an important precious metal source in the North China Craton (NCC; Fig. 1) and is famous for providing gold for royal dynasties for thousands of years. The Jinchangyu gold deposit, located 140 km northeast of Beijing, was first discovered and explored during the Tang Dynasty between 907 and 618 AD. Since 1958, ca. 32 t of gold has been mined with an average grade of 5.30 g/t Au. The gold deposit is one of the largest in eastern Hebei Province with a remaining resource of 20 t of gold at depth.

Red quartz–albite veins host the Jinchangyu Au deposit in an Archean greenstone belt, which consists of the Qianxi–Zunhua Groups. Previous studies have been focused on the geology, ore-controlling structures, geochemistry, mineralogy, and geochronology (Lin et al., 1994; Niu et al., 2012; Song et al., 2011; Yu and Jia, 1989; Zhang et al., 1991), but the timing of the mineralization remains a matter of debate. Some scholars believe that the mineralization is Archean in age (Lin et al., 1994; Wang, 1989; Zhang et al., 1991). Lin et al. (1994) proposed that the deposit was deposited in a ductile shear zone during 2191 ± 58 Ma, based on Ar–Ar dating of quartz from mylonite schist. Luo et al. (2001) argue that the gold is Paleoproterozoic (1858 ± 8 Ma) in age, and others have suggested that the Au mineralization is late Mesozoic (197–169 Ma; Li et al., 2002; Lin and Guo, 1985; Yu and Jia, 1989). Much of the debate relates to the quality of previous data and the limited understanding of the ore genesis and tectonic setting of the deposit.

http://dx.doi.org/10.1016/j.oregeorev.2014.10.031
0169-1368/

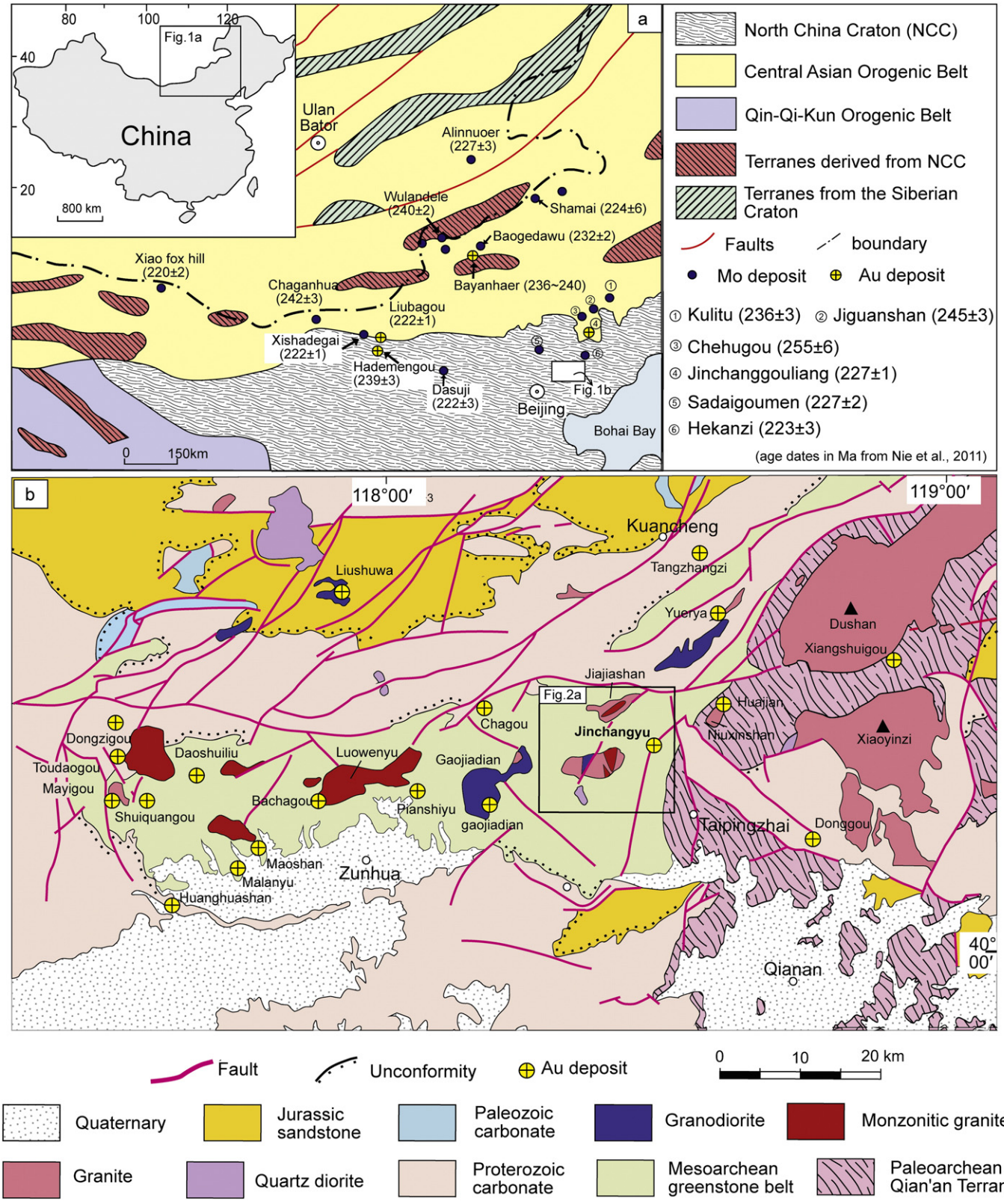

Fig. 1. Simplified geological maps: (a) showing the distribution of Triassic Mo and Au deposits along the northern margin of the North China Craton and adjacent areas (modified after Nie et al., 2011); and (b) East Hebei Province (modified after Mei, 1997).

The red coloration at the Jinchangyu Au deposit is related to alteration associated with the mineralization, but this alteration has not previously been studied. Traditionally, the alteration has been regarded as "red K-feldspathization" or "red albitization" (Lin et al., 1994; Luo et al., 2001; Zhang et al., 1991). The questions of why the albite-quartz veins are red in color, and what the relationship is between the red alteration and the mineralization are important in understanding the genesis of the deposit.

This paper reports new data on the geological and geochemical characteristics of the Jinchangyu Au deposit, in an attempt to elucidate the

relationship between the composition of the red veins and the gold mineralization. In addition, the age of the syngenetic Mo mineralization at the deposit is determined using LA–ICP–MS, which is different when compared to the indirect dating results reported part of the mineralizing system (Li et al., 2002; Lin et al., 1994; Wang, 1989). The results of this study are significant in understanding the ore-forming process and the tectonic setting of the Jinchangyu deposit.

2. Regional geological setting

The Jinchangyu Au deposit is located in eastern Hebei Province in the northeastern part of the NCC (Fig. 1a). Other gold deposits in the region include Yuerya (40° 30′ 00″ N, 118° 31′ 45″ E, 25 t Au, with an average grade of 10.7 g/t Au), Niuxinshan (40° 19′ 40″ N, 118° 32′ 28″ E, 30 t Au, with an average grade of 9.18 g/t Au), Daoliushui, Tangzhangzi, and more than 100 other Mesozoic gold deposits. These deposits make up an important metallogenic belt on the northern margin of the NCC (Hart et al., 2002; Li et al., 2002; Mei, 1997).

Widespread Precambrian rocks host the gold mineralization in the region, including the Jinchangyu Au deposit. Sun (1984) divided the rocks in the region into early Precambrian (Paleoarchean to Paleoproterozoic), Precambrian (Meso- to Neoproterozoic), and Phanerozoic (mostly Mesozoic and Cenozoic) sections. The early Precambrian units are the most extensive and make up the metamorphic crystalline substrate in the craton with rocks as old as ca. 3.5 Ga (Huang et al., 1986; Jahn et al., 1986). These rocks include the Paleo- to Mesoarchean Qianxi and Zunhua groups, which consist of granulite to amphibolite facies mafic to felsic volcanic and sedimentary rocks, and the Qian'an Terrane consisting of granulite successions variably retrogressed to amphibolite facies, with protoliths including calc-alkaline volcanics (Fig. 1b). The geothermal gradient of the region increased during orogenesis in the Neoarchean (Guo et al., 2013), and the changing conditions led to the development of gold mineralization in the greenstone belt. The degree of compression increased from west to east towards the Qian'an Terrane, and gold was remobilized resulting in the formation of large gold deposits in the eastern part of the terrane (Fig. 1; Song et al., 2013), where there was also significant Mesozoic magmatism (Mei, 1997; Nie et al., 2011; Song et al., 2011). Examples of such intrusive bodies include the Qingshankou, Niuxinshan, Yuerya, and Dushan granites, which formed between 245 and 163 Ma at ~20 Ma intervals (Figs. 1b and 2) (Li et al., 2002; Song et al., 2013; Yu and Jia, 1989; Zhang et al., 1991).

The Proterozoic and Paleozoic strata of the region consist of thickly bedded limestone and dolomite, which unconformably overlie the Archean rocks. These include Jurassic volcanic-sedimentary rocks restricted to small continental basins in the northern part of the region (Fig. 1b). Both the basement and the cover sequences have been affected by compressional deformation between the Late Paleozoic and Early Mesozoic (Chen, 1998), when repeatedly deformed regional-scale folds were formed (Zhang et al., 2011). These folds have irregular curved axial traces that trend predominantly eastwards. Archean rocks metamorphosed at deeper crustal levels are exposed as windows in the cores of antiforms, which provided structural controls on both the gold deposits and the Paleozoic to Mesozoic granite intrusions. Faults were formed and reactivated during various periods; these include NE- and NNE-trending transpressional faults and NW-trending transtensional faults; the NNE faults control most of the auriferous veins in the district (Pei and Mei, 2003).

3. Geology of the Jinchangyu gold deposit

3.1. Host rocks

Archean metamorphic rocks are assigned to the Zunhua Group, and host the Jinchangyu Au deposit. The lower units in the group are characterized by amphibolite that hosts the main gold-bearing veins at and around Jinchangyu (Fig. 2a). The amphibolite is dark green in color consisting predominantly of hornblende in association with plagioclase, and minor amounts of clinopyroxene, garnet, quartz, biotite, limonite and pyrite. The rocks are rich in magnesium and iron, but poor in sodium and potassium, containing 48.05–52.92% SiO_2, 14.33–14.98% Al_2O_3, 6.61–13.64% $Fe_2O_3^T$, and 3.41–7.22% MgO (Song et al., 2011). These geochemical characteristics are the same as those of amphibolite units in other parts of eastern Hebei Province (Sun, 1984). The upper units in the group are characterized by thin-layered magnetic quartzite, magnetite-bearing amphibolite, and mafic granulite retrogressed to amphibolite facies. This succession hosts banded iron-ore deposits on the eastern and western sides of Jinchangyu area.

3.2. Structures

The core of the faulted Jinchangyu Anticlinorium hosts the Jinchangyu Au deposit in faults and parasitic folds which trend north-northeast (Figs. 2, 3 and 4). The anticlinorium developed during the Neoarchaean and was originally orientated eastwards (Wang et al., 1985). Shear zones developed along the tight to isoclinal limbs of parasitic folds are characterized by chlorite and sericite schist. These features make the recognition of the folds difficult in the field (Fig. 3).

The Jinchangyu Anticlinorium narrows from north to south, with an undulating axial trace. The gold mineralization is located along the NNE-trending shear zones and fold hinges. The mineralization consists of orebodies arranged *en echelon* along undulations of the parasitic folds at the ground surface. The anticlinorium was uplifted in the south, resulting in erosion of the schistose zones and the occurrence of the orebodies in the tightly folded synclinal cores (Fig. 4a). These orebodies are low grade and limited in depth extent. In the central portion of the deposit, the orebodies are controlled by parasitic anticlines occurring both in fold cores and along their limbs. These orebodies have high Au grades and are open at depth (Fig. 4b).

The Au mineralization formed during a subsequent orthogonal (N–S orientated) compression event resulting in the curvilinear nature of early folds and reactivation of the shear zones as brittle fractures through which gold-bearing fluids were able to permeate (Song et al., 2013). Subsequent eastward trending reverse faults cut the deposit making it difficult to follow them along strike (Fig. 4c).

3.3. Orebodies

The Jinchangyu Au deposit consists of a series of orebodies that extend NNE for ~6 km. The mineralized zone is ~1 km wide and narrows to the north. The main orebodies are divided from west to east into the "0," "i," "ii," "iii," "iv" and "v" zones, of which ii, iii, and v are the richest (Figs. 2b, 4 and 5).

Zone "0" is over several hundred meters long with a limited depth extent in the southwestern part of the deposit. It consists of auriferous veins and lenses that trend northward. Zone "i" is 600 m long, 10–25 m wide, and 180–220 m deep, and trends NE and dips 40°–60° NW. The zone consists of a series of quartz veins averaging 2.87 g/t Au.

Zones "ii," "iii" and "iv" merge at depth (Fig. 4b). Zone "ii" is located in the south-central part of Jinchangyu and contains the main auriferous veins at Jinchangyu. This zone is 890 m long, strikes NNE, dips 60°–80°, is 1–40 m wide, and is >400 m deep. Zone "iii," located to the east of Zone "ii," is over 1 km long and 20 m wide, and dips 60°–80° W. This zone consists of disseminated mineralized sericite schist and quartz–albite veins. It constitutes ≤65% of the total reserves at the Jinchangyu with an average grade of 6.99 g/t Au. Zone "iv" is 700 m long, 10–54 m wide, and 350 m deep. It strikes NNE, dips 70°ESE, and has low Au grades (Fig. 4).

Zone "v" is located in the hanging wall of a transpressional fault locally referred to as "F_{19}." It is currently being explored with an average grade of 5.93 g/t Au to date. The zone is 1500 m long, 45 m wide, and 1000 m deep, trends NE and dips 70°–85° W (Fig. 5).

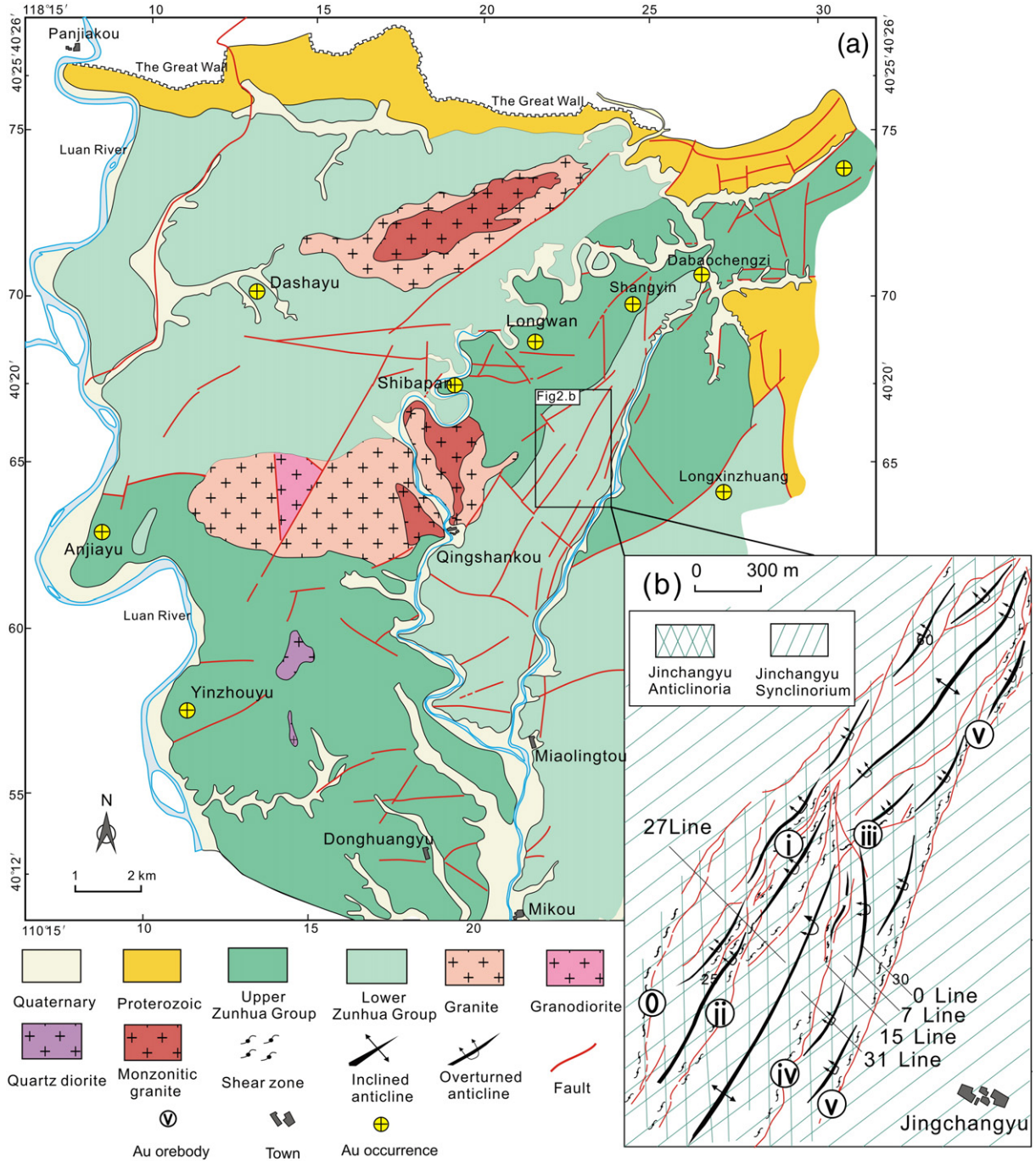

Fig. 2. Geological maps of: (a) the Jinchangyu region; and (b) the Jinchangyu Au–Mo deposit (modified after Song et al., 2011).

3.4. Metallogenic stages and alteration assemblages

On the basis of the mineral assemblages and crosscutting relationships, at least four paragenetic stages have been recognized. Stage I, the oldest red assemblage consisting of quartz–albite–hematite (Q–Al–Hem), contains minor gold and molybdenite (Fig. 6a and b). Stage II, the pink veins consisting of quartz–albite–hematite (Q–Al–Hem), contains quartz–albite–polymetallic sulfides (Q–Al–Poly). The veins are commonly auriferous containing native gold pyrite, molybdenite, chalcopyrite, magnetite, and minor amounts of galena, and sphalerite (Fig. 6b, c, d and e). The Stage III assemblage consists of quartz–pyrite (Q–Py) veins that are characteristically wide and locally containing native gold (Fig. 6f). Stage IV quartz–carbonate (Q–Cal) veins are generally not mineralized and crosscut the earlier stages (Fig. 6g and h).

Most of the albite and quartz was formed during the protomylonite–mylonite deformation in Stages I and II (Fig. 6i). Albite sometimes shows a porphyroclastic texture with semi-plastic deformation, and quartz shows the effect of dynamic recrystallization with many small inclusions derived from the adjacent country rock (Fig. 6j). Gold was mostly introduced during the formation of Stage II. The native gold in Stage II is irregular in shape and hosted in fractures, and crystal faces of pyrite and molybdenite (Fig. 6k–m). Molybdenite is also abundant at Jinchangyu, with a resource of 864 t with an average grade of

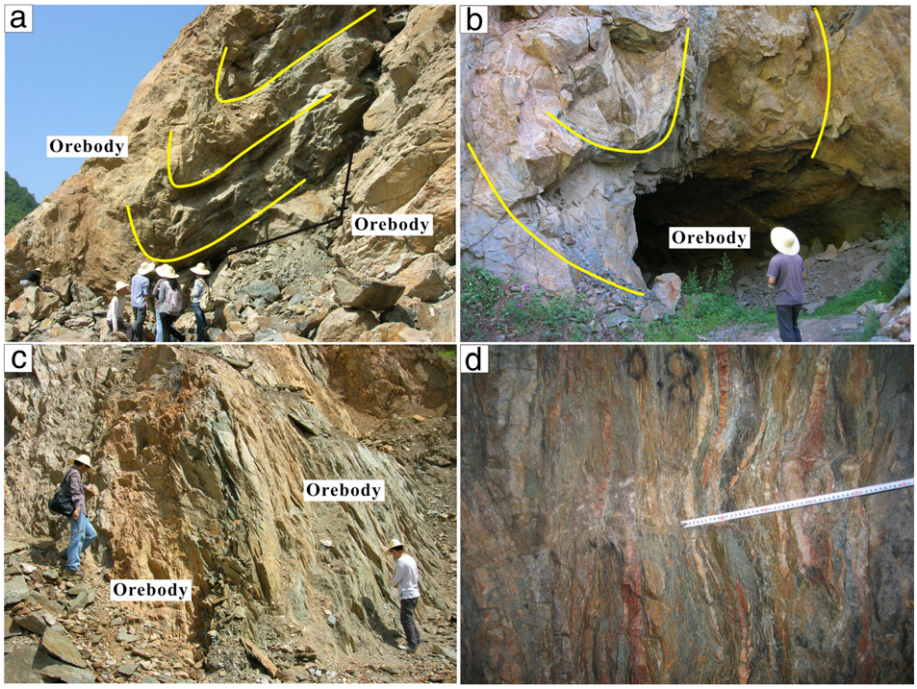

Fig. 3. Photographs showing the occurrences of orebodies: (a) and (b) in fold hinges; (c) steeply dipping orebodies in fold limbs; and (d) well developed schistosity of the host rocks.

0.071% Mo and a minimum mining thickness of 2 m (Luo et al., 2001). The molybdenite is associated with gold-bearing pyrite in the form of veinlets or disseminations in quartz veins (Fig. 6e, l and m).

Alteration associated with Au mineralization at Jinchangyu is confined to the anticlinorium and is characterized by sericite, chlorite, silica, sulfides, carbonate, and albite. Judging from the gradual progression from unaltered amphibolite to chlorite schist, Fe_2O_3, CaO, and MgO have been removed during the alteration (Song et al., 2011).

4. Quartz–albite–hematite veins

Quartz–albite–hematite veins range from dark to light in color and some of the assemblages have a bleached white appearance. The "red alteration" was observed as red veins in the field, which are generally 50–700 mm wide and were emplaced along schistose zones and in fold hinge zones (Fig. 6a). Some red veins are dark in color and display a strong ductile fabric, whereas others are light in color and are weakly

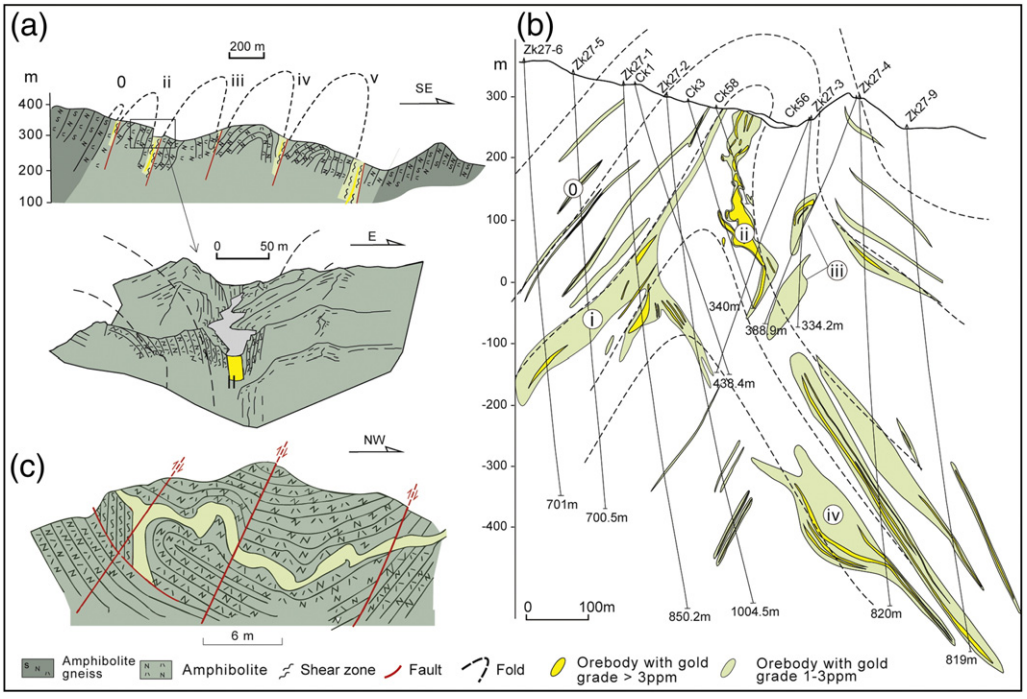

Fig. 4. Geological sections: (a) the southern part of the Jinchangyu Au–Mo deposit (modified after Song et al., 2011); (b) no. 27 exploration line across the major gold orebodies; and (c) showing post-mineralization faults.

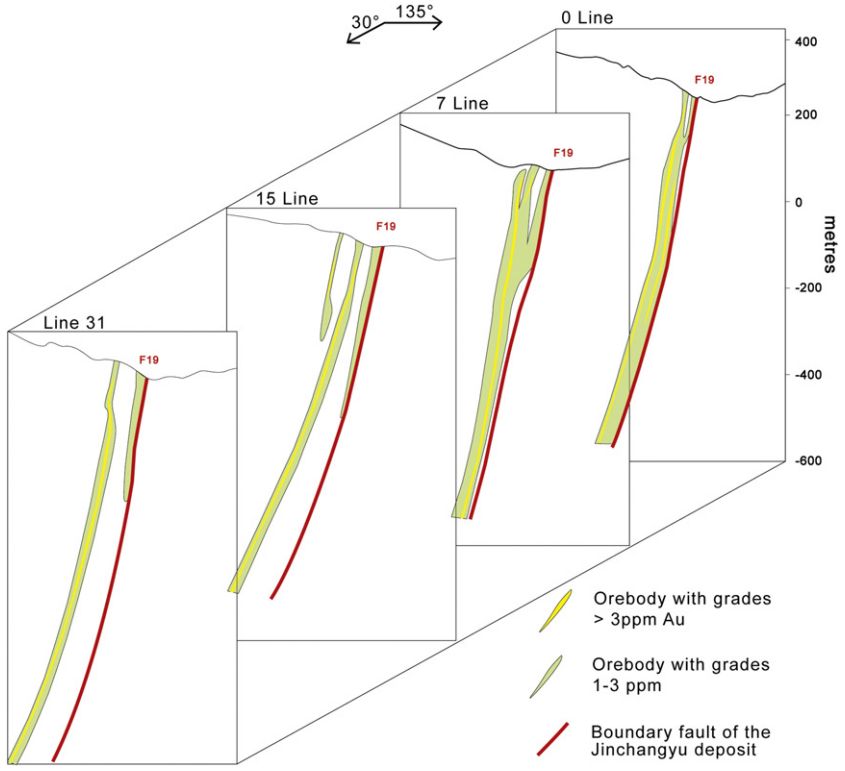

Fig. 5. Three dimensional model of orebody "v" at the Jinchangyu Au–Mo deposit based on section lines 0 to 31 (modified after Lin et al., 1994).

deformed. Light red (pink) quartz veins are always associated with gold-bearing sulfides and native gold (Fig. 6).

Electron probe micro-analysis (EPMA) and microprobe Raman spectroscopy were used to determine the composition of the red veins. Under the microscope, the groundmass of the red veins is white and light gray, which is significantly different when compared to that observed with the naked eye, and the hematite crystals are distributed as maroon spot (Fig. 6). White substrates, which clearly show polysynthetic twinning (Fig. 6), are composed of quartz (>85%) with small amounts of albite (<5%). The EPMA results show that the chemical composition of the samples (Table 1) is 11.1% Na_2O, 19.7% Al_2O_3 and 68.5% SiO_2, which is consistent with a sodium aluminum silicate ($NaAlSi_3O_8$) composition. Therefore, it can be concluded that the feldspar minerals in the Jinchangyu gold-bearing veins are dominated by albite (99%).

A comparison of the peaks of feldspar from Jinchangyu and the peaks of red plaques with the RRUFF mineral spectral database (https://rruff-2.geo.arizona.edu/; Fig. 7a and b) indicates that the red plaques are hematite. The dark red color of veins and the pink quartz–albite veins have varying amounts of hematite.

5. Samples and analytical methods

Seven molybdenite samples were collected from different depths in the Jinchangyu deposit for dating using the Re–Os method. All samples were obtained by crushing ore samples from gold-bearing quartz–albite veins, separating out molybdenite using heavy liquid techniques, and carefully handpicking under a microscope to remove accreted pyrite and other impurities (resulting in a purity >99%). Fine-grained (<0.1 mm) molybdenite was sampled to avoid Re and Os decoupling within large molybdenite grains (Selby and Creaser, 2004; Stein et al., 2003).

Re–Os isotope analyses were performed in the Re–Os Laboratory of the National Research Center of Geoanalysis, Chinese Academy of Geological Sciences (CAGS), Beijing, China. The instrument used was an ICP–MS (TJA X-series, Thermo Electron Corporation, USA). The analytical procedures followed the methodology described by Shirey and Walker (1995) and Du et al. (2004). Model ages were calculated using the equation $t = [\ln(1 + {}^{187}Os/{}^{187}Re)]/\lambda$, where λ is the decay constant of ^{187}Re of $1.666 \times 10^{-11} \cdot a^{-1}$ (Smoliar et al., 1996).

Petrographic, microthermometric, and laser Raman spectroscopic studies of fluid inclusions were carried out at the Key Laboratory of Lithospheric Evolution, Institute of Geology and Geophysics, Chinese Academy of Sciences. Quartz samples were prepared as doubly polished wafers with a thickness of 150 μm. Microthermometry experiments were carried out using a Linkam LMS600 heating-freezing stage attached to a microscope. The stage was regularly calibrated using FLINCOR synthetic standards of pure CO_2 (triple point of −56.6 °C) and H_2O (critical point of 372.4 °C; melting temperature at −0.2 °C) fluid inclusions. Heating rates of 1 °C/min were employed for measurements below 30 °C and 5 °C/min up to 400 °C. Consequently, the accuracy of the measurements was approximately ±0.2 °C during the freezing cycle and ±2 °C during heating measurements. Fluid inclusions were analyzed using a Renishaw RW-2000 Laser Raman microspectrometer. The laser source was an argon ion laser with a wavelength of 514.5 nm. The spectral range falls between 100 cm^{-1} and 4000 cm^{-1}.

H–O–S isotopes were analyzed in the Analytical Laboratory of the Beijing Research Institute of Uranium Geology, China, using a Finnigan MAT253 mass spectrometer. Thirty-six quartz samples from quartz–albite veins (Stage II) and quartz–pyrite veins (Stage III) were analyzed. Oxygen was liberated from quartz by reaction with BrF_5 and converted to CO_2 on a platinum-coated carbon rod for oxygen isotope analysis. The water of the fluid inclusions in quartz was released by heating the samples to above 500 °C in an induction furnace, and then reacting with zinc powder at 410 °C to generate hydrogen for isotope analysis. The results were reported in per mil (‰) relative to SMOW standards, with precisions of ±2‰ for δD and ±0.2‰ for $\delta^{18}O$.

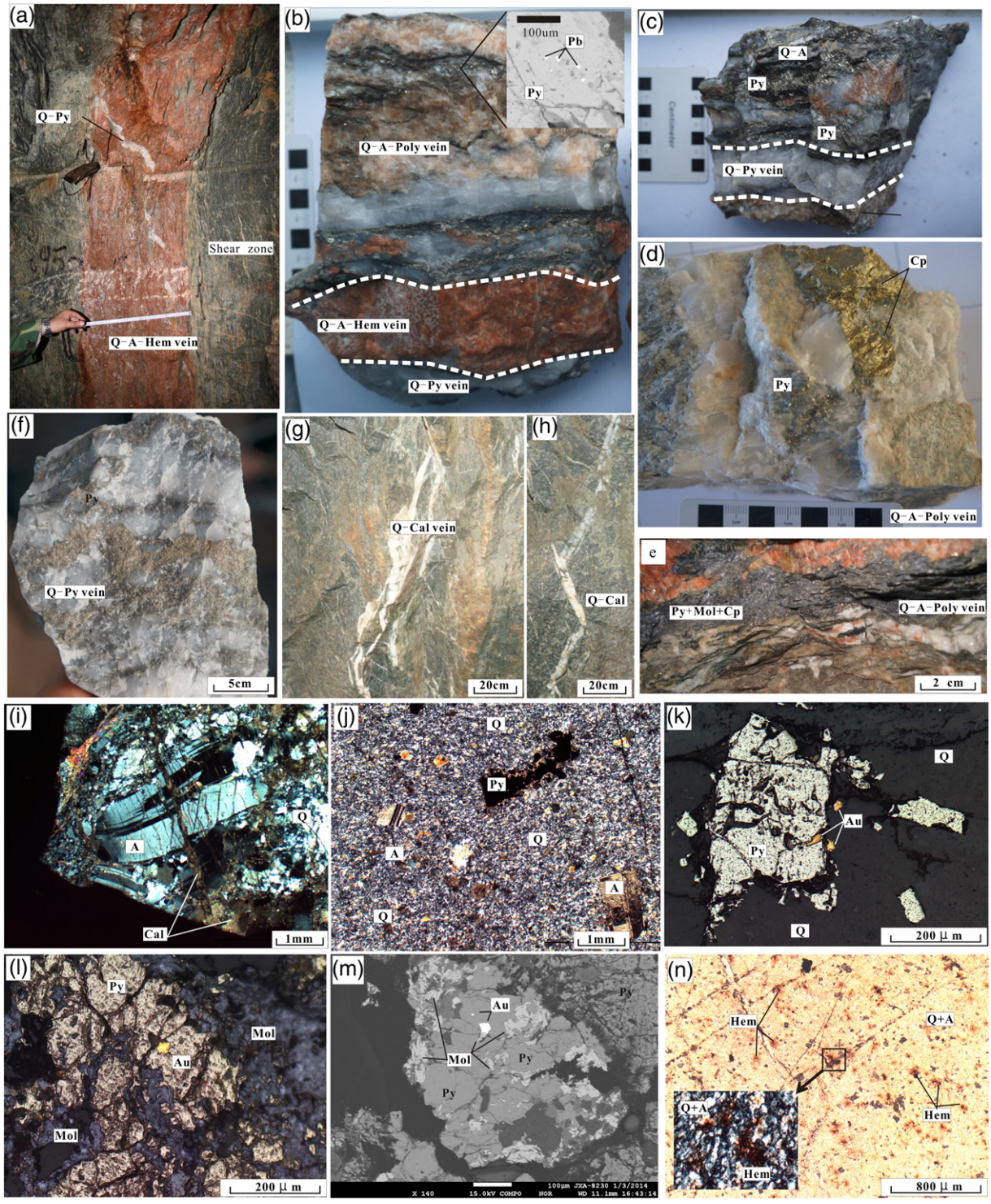

Fig. 6. Photographs (a) to (h) of field and hand samples of ore from different stages of veins and mineral assemblages. Photomicrographs (i to n) of veins and ore, including SEM backscattered electron image of ore (m). In detail: (a) Stage I sheet-like red veins cut through by a later quartz vein; (b) red sulfide-poor quartz–albite vein cut by a quartz–albite–polymetallic sulfides vein; (c) Stage II pink quartz–albite–polymetallic sulfides veins cut by Stage III quartz–pyrite veins; (d) chalcopyrite and pyrite in a Stage II pink vein; (e) Stage II pyrite–molybdenite aggregates; (f) Stage III quartz–pyrite veins; (g) and (h) Stage IV quartz–carbonate veins; (i) deformed albite; (j) albite and pyrite in red veins; (k) occurrence of native gold in pyrite and quartz; (l) native gold enclosed in pyrite; (m) SEM backscattered electron image of native gold, pyrite, and molybdenite; and (n) hematite in red veins. Abbreviations: Qt = quartz, A = albite, Cal = calcite, Py = pyrite, Cp = chalcopyrite, Mol = molybdenite, Pb = galena, Au = native gold, Hem = Hematite.

Forty-three pyrite samples were obtained from different depths for S isotope analysis, and the separated sulfide minerals were crushed to 200 mesh. Sulfur isotopic ratios were measured with a Finnigan MAT-251EM mass spectrometer. The results are reported for standards and for the separated troilite In Table 5. The reproducibility of $\delta^{34}S$ values is ±0.2‰.

6. Results

6.1. Re–Os dating

The results of molybdenite Re–Os dating are listed in Table 2. The Re range from 289.1 to 9643 ppb, and ^{187}Os range from 0.6913 to

Table 1
The chemical composition (wt.%) and structural formula of albite in the red veins in Jingchangyu Au–Mo deposit.

Element	Samples													
	J326-1	J326-2	J326-3	J326-4	J326-5	J257-1	J257-2	J257-3	J257-4	J257-5	J23-1	J23-2	J23-3	J23-4
SiO_2	68.26	68.63	68.36	68.12	69.20	68.61	68.87	68.48	68.22	68.49	68.62	68.00	68.59	68.68
Al_2O_3	19.62	20.03	19.64	19.22	19.34	19.16	19.64	19.53	19.98	20.05	19.89	20.38	19.81	20.07
CaO	0.04	0.01	0.02	0.02	0.02	0.01	0.11	0.04	0.05	0.03	0.01	0.04	0.02	0.03
Na_2O	10.89	11.04	11.23	11.49	11.81	11.55	11.00	11.30	11.28	11.38	10.42	9.72	11.34	11.09
K_2O	0.04	0.04	0.03	0.02	0.01	0.05	0.06	0.07	0.02	0.04	0.39	1.01	0.06	0.05
P2O5	0.05	0.00	0.00	0.03	0.04	0.00	0.00	0.00	0.01	0.03	0.00	0.03	0.05	0.00
MgO	0.02	0.01	0.00	0.01	0.00	0.00	0.00	0.00	0.00	0.00	0.00	0.00	0.00	0.00
MnO	0.03	0.02	0.01	0.00	0.02	0.00	0.00	0.00	0.00	0.00	0.05	0.00	0.02	0.00
FeO	0.30	0.31	0.34	0.36	0.27	0.00	0.01	0.00	0.00	0.04	0.14	0.08	0.06	0.03
TiO2	0.00	0.00	0.00	0.00	0.03	0.00	0.00	0.00	0.00	0.00	0.00	0.01	0.01	0.00
Si	3.003	2.994	2.999	3.004	3.008	3.010	3.006	3.001	2.986	2.986	3.004	2.987	2.994	2.992
Al	1.018	1.030	1.015	0.999	0.991	0.991	1.010	1.009	1.031	1.030	1.026	1.055	1.019	1.030
Ca	0.002	0.000	0.001	0.001	0.001	0.001	0.005	0.002	0.002	0.002	0.000	0.002	0.001	0.002
Na	0.929	0.934	0.956	0.983	0.995	0.982	0.931	0.961	0.958	0.962	0.884	0.828	0.960	0.937
K	0.002	0.002	0.002	0.001	0.000	0.003	0.003	0.004	0.001	0.002	0.022	0.056	0.004	0.003
An	0.210	0.030	0.070	0.090	0.100	0.060	0.550	0.190	0.250	0.160	0.040	0.200	0.090	0.170
Ab	99.530	99.750	99.770	99.800	99.850	99.680	99.110	99.420	99.610	99.590	97.570	93.450	99.540	99.520
Or	0.260	0.210	0.150	0.110	0.040	0.260	0.340	0.390	0.140	0.250	2.380	6.360	0.370	0.310

An: anorthite; quartz; Or: orthoclase; Ab: albite.

23.54 ppb. Seven samples have a Re–Os model age of 219 to 233 Ma and a weighted mean age of 225 ± 4 Ma (Fig. 8a), and the processed data indicate an isochron age of 223 ± 5 Ma (Fig. 8b). The nearly identical model age and isochron age indicate that the analytical results are reliable.

6.2. Fluid inclusions

6.2.1. Fluid inclusion petrography

Fluid inclusions were selected from the gold-bearing quartz–albite veins (Stage II) and quartz–pyrite veins (Stage III) for microthermometric measurements. Based on the petrographic and compositional features of the inclusions at room temperature and their Raman characteristics, three types of inclusions were recognized in the quartz from Stage II and Stage III veins (Fig. 9); we refer to these as the aqueous two-phase CO_2–H_2O fluid inclusions with daughter mineral-bearing inclusions.

The aqueous two-phase inclusions (W-type) are presented in the Stage II and III quartz veins and are characterized by a vapor bubble in an aqueous liquid at room temperature. They typically have irregularly ellipsoidal shapes with a vapor volume accounting 5–15 vol.% and are generally between 4 and 12 μm in size. They are interpreted as having a primary origin, and usually have a higher vapor/liquid ratio than secondary inclusions.

The CO_2–H_2O fluid inclusions (C-type) are characterized by irregular or negative crystal shapes and are located in the gold-bearing quartz–albite veins (Stage II) and quartz–pyrite veins (Stage III). Fluid

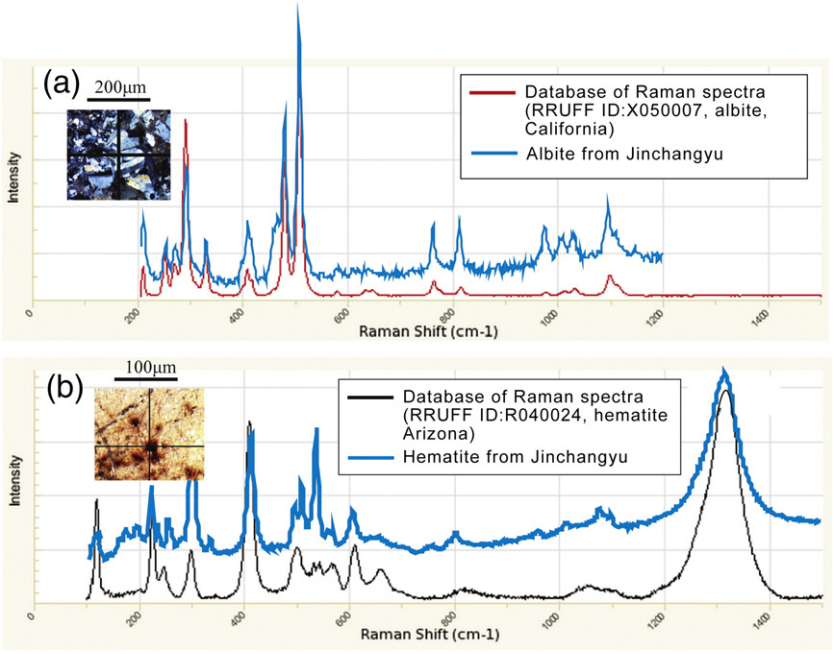

Fig. 7. Representative Raman spectra of: (a) albite; and (b) hematite in the Jinchangyu red veins.

Table 2
Re–Os isotopic data for molybdenite.

Sample no.	Sampling location	Weight (g)	$w_{(Re)}$/ppb		$w_{(Os)}$/ppb		$w_{(^{187}Re)}$/ppb		$w_{(^{187}Os)}$/ppb		Age (Ma)	
			Measure	2σ	Measure	2σ	Measure	2σ	Measure	2σ	Age	2σ
J257-22	−257 Level,25 line	0.00669	7038	39	0.0531	0.0003	4423	25	16.20	0.07	219.4	2.6
J257-23	−257 Level, 19line	0.03318	4747	20	0.7184	0.0023	2984	13	11.10	0.04	222.8	2.5
J417-19	−417 Level,27 line	0.02030	9643	80	0.0246	0.0004	6061	50	23.54	0.10	232.7	3.1
J103-6	103 Level,07 line	0.00278	2642	9	0.1524	0.0005	1660	6	6.147	0.025	221.8	2.5
J23-11	23 Level,17 line	0.05083	325.6	2.7	0.0133	0.0058	204.6	1.7	0.7664	0.0109	224.4	4.1
J23-12	23 Level,17 line	0.05033	289.1	0.9	0.0145	0.0002	181.7	0.6	0.6913	0.0028	227.9	2.5
JM-6	23 Level,31 line	0.05355	536.0	4.4	0.0131	0.0012	337.03	2.87	1.291	0.011	229.5	3.2

inclusions within this group are generally 3–10 μm in size and consist of two (liquid water + liquid CO_2) or three (liquid water + liquid CO_2 + CO_2-rich vapor) phases at room temperature. The CO_2 vapor in some CO_2–H_2O fluid inclusions occupies 10–85 vol.%. All of the CO_2–H_2O inclusions are considered to be primary in origin.

The daughter mineral-bearing inclusions (S-type) are round, negatively shaped, and isolated, with sizes varying between 6 and 10 μm. The daughter minerals are dominated by cubic-shaped halite.

6.2.2. Fluid inclusion microthermometry

Auriferous quartz veins are abundant in a large part of eastern Hebei Province, indicating the presence of a large mineralizing system in the region. The homogenization temperatures (from 265° to 370 °C) and decrepitation temperatures (from 124° to 325 °C) reported for fluid inclusions in auriferous quartz veins (Yu and Jia, 1989; Zhong et al., 1996).

6.2.2.1. Gold-bearing quartz–albite veins (Stage II). The W-type inclusions are usually found near C-type fluid inclusions, with $T_{m\text{-}ice}$ of −4.5° to −2.4 °C. Homogenization of the liquid phase takes place between 210° and 355 °C with an estimated salinities range from 4.01 to 7.05 wt.% NaCl equivalent. The vapor phase of these fluid inclusions consists of 93.79–99.07 mol % H_2O and 0.75–5.48 mol % CO_2, and Yu and Jia (1989) reported that the liquid phase is dominated by H_2O containing Na^+, K^+, Ca^{2+}, Cl^- ions.

The melting temperature of solid CO_2 ($T_{m\text{-}CO2}$) ranges from −56.6° to −58.3 °C, with a mode at −57.1 °C, which is slightly below the triple point of pure CO_2 (−56.6 °C). The melting temperatures of clathrates ($T_{m\text{-}cla}$) were observed to be between 6.0° and 8.5 °C, indicating that the salinities are 3.0–7.48 wt.% NaCl equivalent. The CO_2 vapor ($T_{h\text{-}CO2}$) was partially homogenized to liquid at temperatures ranging from 27.8° to 32.5 °C. Total homogenization ($T_{h\text{-}tot}$) of the CO_2 vapor and aqueous phases was observed at temperatures ranging between 265° and 410 °C. The calculated CO_2 densities range from 0.69 to 0.85 g/cm^3. Raman analysis shows that the volatile component of these fluid inclusions is dominated by CO_2 and H_2O.

A few S-type fluid inclusions were observed to homogenize in the liquid phase in the quartz–albite veins at temperatures of 366° and 389 °C. The daughter halite in these inclusions dissolved at temperatures between 85° and 110°, indicating salinities of 27.6–28.3 wt.% NaCl equiv.

The homogenization statistics in Fig. 10 was observed at temperatures ranging between 210° and 410 °C; however, the peak of $T_{h,tot}$ is between 270° and 350 °C (Table 3).

6.2.2.2. Quartz–pyrite veins (Stage III). Fluid inclusions in the quartz–pyrite veins are dominantly W-type. The $T_{m\text{-}ice}$ of the W-type aqueous inclusions is between −8.9° and −2.7 °C (Table 3), corresponding to salinities of 4.79–12.53 wt.% NaCl equivalent. Homogenization in the liquid phase happens at temperatures between 120° and 320 °C, which are lower than those of the Stage II (Fig. 10a).

The melting temperatures of solid CO_2 ($T_{m\text{-}CO2}$) range from −56.6° to −57.0 °C, and the observed melting temperatures of clathrates ($T_{m\text{-}cla}$) are between 4.3° and 8.0 °C, indicating that the salinities are 3.95–10.14 wt.% NaCl equivalent. Total homogenization ($T_{h\text{-}hot}$) of the carbonic and aqueous phases was observed at temperatures between 260° and 340 °C (Fig. 10b), lower than those of the Stage II. The calculated CO_2 densities range from 0.71 to 0.75 g/cm^3.

Total homogenization was observed at temperatures ranging between 120° and 340 °C; cluster between 180° and 240 °C (Fig. 10).

6.2.3. Laser Raman spectra

Representative samples were examined using laser Raman microspectroscopy to determine the composition of fluid inclusions. The data show that CO_2 and H_2O are the main volatiles in the inclusions from the stage II and III quartz, and small quantities of CH_4 and N_2 are present in samples from gold-bearing quartz–albite veins (Fig. 11).

6.3. H–O isotopes

Oxygen and hydrogen isotopic compositions of fluid inclusions collected from different stages and the oxygen isotope compositions of

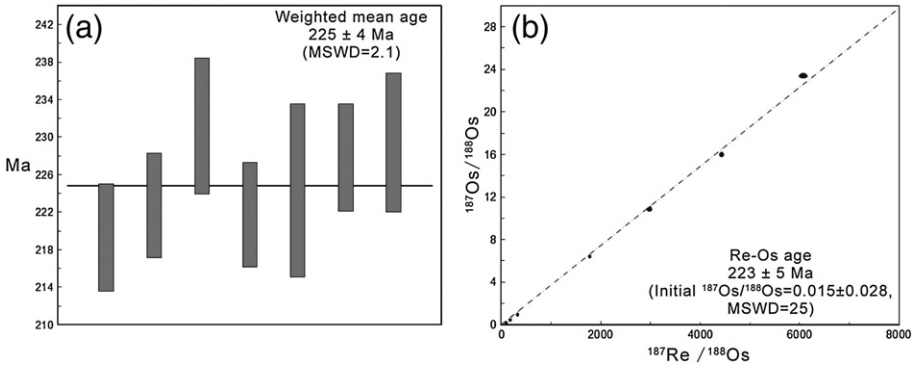

Fig. 8. Re–Os weighted mean age (a) and isochron plot (b) of molybdenite samples from the Jinchangyu deposit.

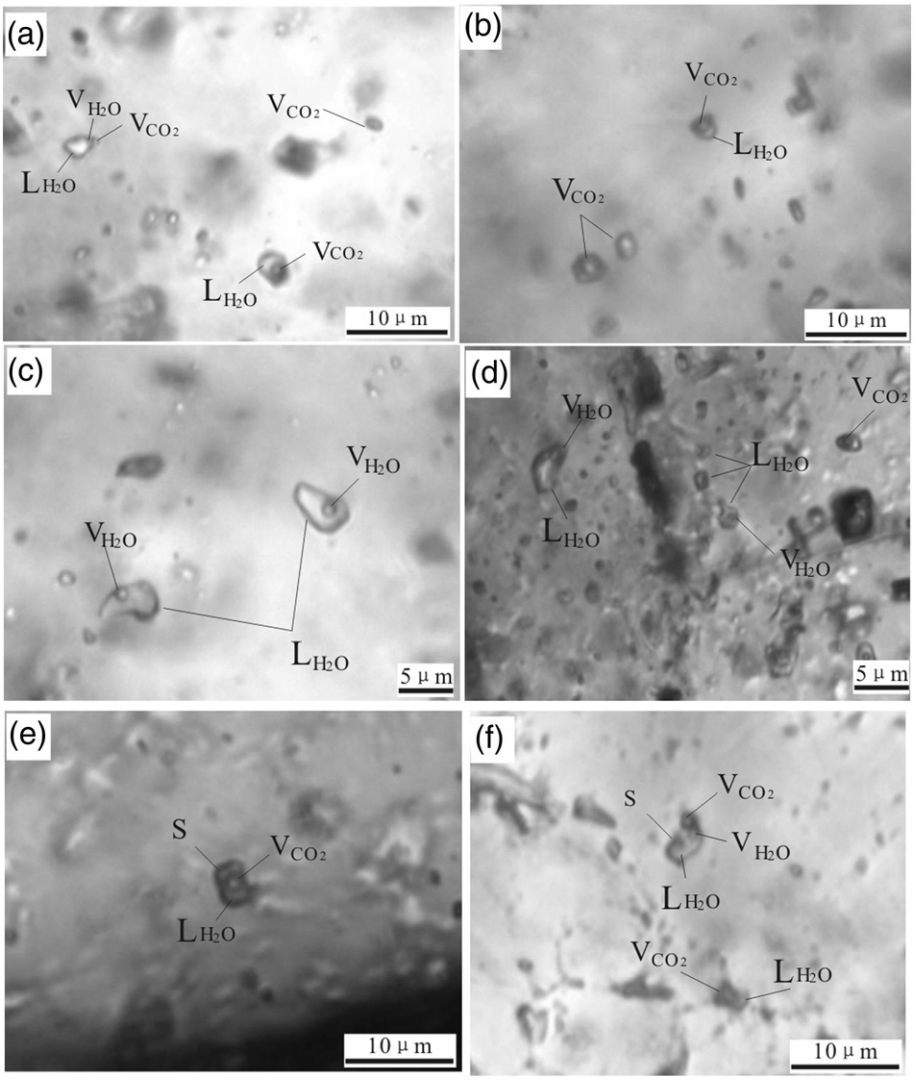

Fig. 9. Photomicrographs showing: (a) two-phase and three-phase CO_2–H_2O inclusions and vapor CO_2 inclusions; (b) CO_2-rich and CO_2–H_2O inclusions coexisting with primary two-phase aqueous inclusions; (c) H_2O–NaCl two-phase fluid inclusions; (d) aqueous two-phase inclusions coexisting with CO_2–H_2O inclusions; (e) isolated daughter mineral(S)-bearing inclusion; and (f) daughter mineral(S)-bearing multiphase inclusions coexisting with CO_2–H_2O inclusions.

some rock samples from the mineralized area are listed in Table 4. The oxygen isotopic compositions of hydrothermal fluids in equilibrium with quartz were calculated using an extrapolation of the fractionation formula ($1000\ln\alpha_{quartz\text{-}H2O} = 3.38 \times 10^6 T^{-2} - 3.40$) from Clayton et al. (1972). Calculations of the fractionation factors were performed using the mean value of the homogenization temperatures of fluid inclusions plus pressure-corrected temperatures, as discussed below. The calculated O isotopic composition of the fluid in Stage II varies from 2.0 to 6.4‰, and the O isotope values of Stage III vary between −0.9 and 4.3‰. The analyses of the H isotopic composition, measured directly in inclusion fluids, give a range of δD, between −83.9 and −54.8‰.

6.4. S isotopes

The $\delta^{34}S$ values (Table 5) for pyrite in red quartz–albite veins (Stage I) range from −4.1 to 0.8‰, and the $\delta^{34}S$ values of pyrite and molybdenite in pink quartz–albite veins (Stage II) range from −4.1 to 1.8‰. Five samples of molybdenite have $\delta^{34}S$ values between −2.3 and 1.8‰. The $\delta^{34}S$ values for pyrite from Stage III quartz veins range from −4.4 to 5‰.

7. Discussion

7.1. The source of ore-forming materials and fluids

The average $\delta^{34}S$ value for sulfide minerals can represent the total sulfur in the hydrothermal fluid for simple mineral associations (Hoefs, 1997). Pyrite and molybdenite make up more than 90% of all the sulfides in the Jinchangyu Au deposit. Most of the $\delta^{34}S$ values determined on pyrite and molybdenite in the deposit are between −4.4 and 1.9‰. Apart from the anomalous value of 5‰ from sample JK323-5, the pyrite values approximately represent the total $\delta^{34}S$ range values of the ore-forming fluids, which is narrow and close to zero (Fig. 12). This indicates that the mineralization was associated with magmatic activity (Hoefs, 1997). Thirteen $\delta^{34}S$ values reported by Zhang et al. (1991) and Yu and Jia (1989) from the wall-rock amphibolite at the deposit clustered between −1.2 and 5.2‰, which partially overlap with the cluster for the ore-hosting rocks in Fig. 12. From this we can conclude that the sulfur in the ore-forming fluids was mostly derived from a magmatic source with some input from the host Precambrian metamorphic rocks.

The Pb isotope ratios for the sulfide minerals in host rock and Qingshankou Granite near Jinchangyu (Lin and Guo, 1985) overlap

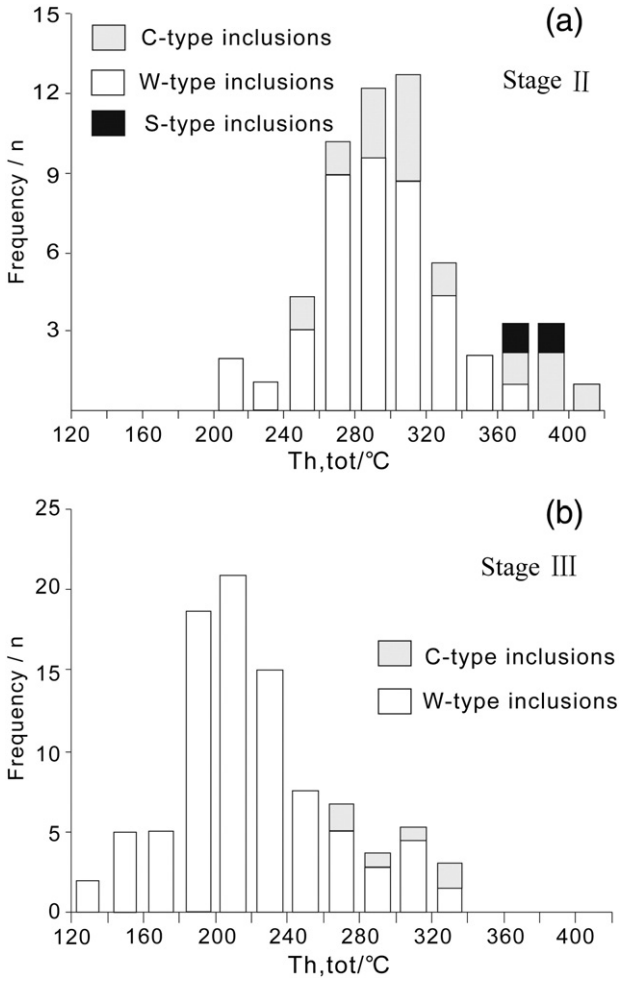

Fig. 10. Histograms of thermometric measurements of fluid inclusions; (a) Stage II veins, (b) Stage III veins.

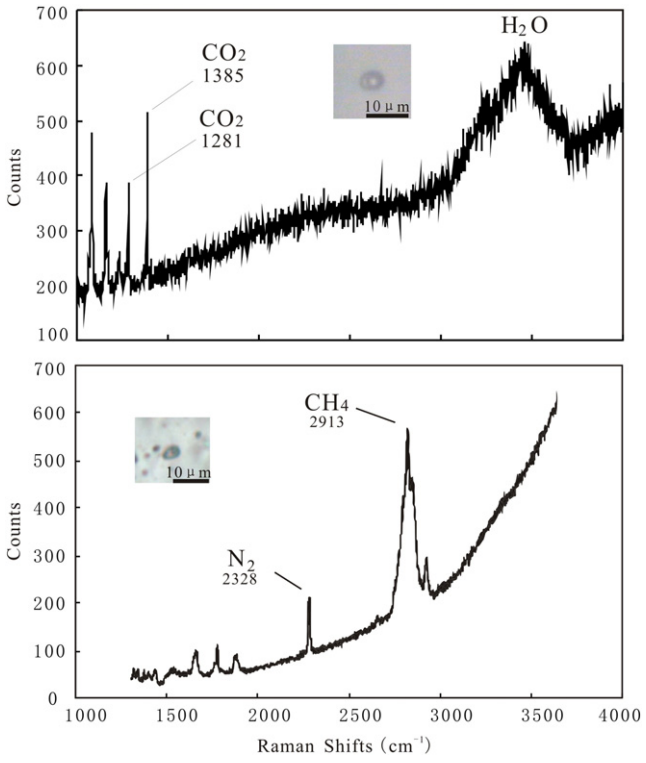

Fig. 11. Representative Raman spectra of vapor bubbles of fluid inclusions in gold-bearing quartz–albite veins.

with the range in lower crustal values of Zartman and Haines (1988) (Fig. 13). This indicates that the Pb reservoirs for these components have similar Pb sources, and the Jinchangyu ore and the Mesozoic Qinshankou magmatic rocks have similar origins and have interacted with the Precambrian country rocks.

As discussed earlier, the peak of homogenization temperature of fluid inclusions from the auriferous quartz–albite veins (Stage II) at Jinchangyu is between 270° and 350 °C, and the peak homogenization temperature of fluid inclusions in the Stage III quartz–pyrite veins ranges from 180° to 240 °C. These mineralized fluids are H_2O–CO_2-bearing, with low to moderate salinities, which are typical of the majority of Archean and Phanerozoic mesothermal vein-style gold deposits in greenschist-facies terranes (Fan et al., 2003; Gebre-Mariam et al., 1995; Kolb and Meyer, 2002). Although many of these deposits have been attributed to formation by metamorphic processes (e.g. Goldfarb et al., 1988; Witt et al., 1997), models requiring magmatic sources or evolved meteoric fluids have also been proposed for the deposits with formation at sub-greenschist to greenschist facies (e.g. Fan et al., 2003; Kolb and Meyer, 2002; Pirajno and Bagas, 2008; Zhang et al., 2005).

The δD_{H2O} and $\delta^{18}O_{SMOW}$ values for the quartz–albite–polymetallic sulfide (Stage II) veins and quartz–pyrite (Stage III) veins at Jinchangyu have a narrow range. The calculated $\delta^{18}O_{H2O}$ values based on the average homogenization temperatures of fluid inclusions in the two stages are significantly different, from +2.0 to +6.4‰ in the Stage II (quartz–albite veins) and from −0.9 to +4.3‰ in the Stage III (quartz-sulfide) veins. Fluids in the Stage II veins are closer to magmatic fluid and lead in the direction of meteoric water for the Stage III veins (Fig. 14), which indicates that the ore-forming fluids have a mixed magmatic and meteoric source. Zhang et al. (1991) document that the ore-forming fluid inclusions at Jinchangyu have a $\delta^{13}C_{CO2}$ range of −8.44 to −2.27‰, which also indicates that the carbon in the Jinchangyu mineralizing fluid was largely derived from a magmatic source (magmatic carbon $\delta^{13}C_{PDB}$ = −8 to −5‰; Hoefs, 1997).

The initial Os isotope ratio can provide significant information on the source of the ore-forming materials (Schaefer, 2004). Generally,

Table 3
Microthermometric data on fluid inclusions in the Jinchangyu Au–Mo deposit.

Veins/stage	Inclusions type	$T_{m,CO2}$/°C	$T_{m,cla}$/°C	$T_{h,CO2}$/°C	$T_{m,ice}$/°C	$T_{m,s}$/°C	$T_{h,tot}$/°C	TD	Salinity (wt.% NaCl equiv.)	CO2 density (g/cm^3)
Q–Al–Poly Stage II	C	−56.6 to −58.3	6.0–8.5	27.8–32.5			265–410		3.0–7.48	0.69–0.85
	W				−4.5 to −2.4		210–355		4.01–7.15	0.65–0.90
	S					85–110	360–380	380–400	27.6–28.3	0.90–0.93
Q–Py Stage III	W				−2.9 to −8.7		120–320		4.79–12.53	0.75–0.96
	C	−56.6 to −57.0	4.3–8.0	22.5–26.6			260–340		3.95–10.14	0.71–0.75

$T_{m,CO2}$ = final melting temperature of solid CO_2. $T_{m,cla}$ = final melting temperature of the clathrate phase. $T_{h,CO2}$ = homogenization temperature of CO_2 phase. $T_{m,ice}$ = final melting temperature of water ice. $T_{m,s}$ = final melting temperature of daughter mineral. TD = decrepitation temperature. $T_{h,tot}$ = temperature of total homogenization of the inclusions. wt.% NaCl equiv. = weight percent NaCl equivalent.

Table 4
Oxygen and hydrogen isotope compositions of fluid inclusions in quartz from the Jinchangyu Au–Mo deposit.

Sample no.	$\delta^{18}O_{SMOW}$ (‰)	$\delta^{18}O_{H2O}$ (‰)	δD_{H2O} (‰)
The pink quartz–albite vein (Stage II), Th (°C) = 310			
Mineral analyzed: quartz			
JK316-2	12.9	5.9	−65.5
JK318-1	13.4	6.4	−64.5
JK301-10	12.1	5.1	−74
JK302-1	11.4	4.4	−67.8
JK303-3	12.1	5.1	−74.8
JK303-8	11	4	−69.4
JK307-2	13	6	−72.3
JK308-7	12.7	5.7	−73.9
JK63-37-9	11.2	3.5	−70.6
JK310-9	12.5	2	−62.6
JK310-10	12.7	5.7	−65.6
JK312-9	13.2	6.2	−75.3
JK314-2	12.9	5.9	−56.1
JK319-7	12.2	3.9	−67.4
JK319-8	12.6	5.6	−67.6
JK324-11	12.9	5.9	−70.2
JK326-4	12.7	5.7	−70
JK326-5	12.5	5.5	−69.4
JK328-2	13	6	−71.1
JK308-8	12.9	5.9	−71.4
JK311-5	12.9	5.9	−69.6
JK327-6	12	5	−67.5
The quartz–pyrite veins (Stage III), Th (°C) = 205			
Mineral analyzed: quartz			
JK17-23	11	−0.9	−83.9
JK17-23-5	11.9	0	−60
JK320-6	13.2	1.3	−64.9
JK322-7	13.1	1.2	−63.5
JK323-5	11.9	0	−78.1
JK324-10	11.4	−0.5	−67.2
JK305-7	12.6	3.7	−55.7
JK316-7	11.7	−0.2	−70.8
JD327-5	12.7	0.8	−67.1
JD325-2	16.2	4.3	−67
JK103-37-3	12.6	0.7	−68
JK103-37-H1	11.4	−0.5	−54.8
JK63-37-4	11	−0.9	−65.4
JK304-1	12.1	0.2	−57
JK304-2	12.7	2.1	−78.4

$1000\ln\alpha_{quartz\text{-}H2O} = 3.38 \times 10^6\ T^{-2} - 3.40$.

the initial Os value from the mantle is very low with the $^{187}Os/^{188}Os_{(i)}$ ratio ranging from 0.12 to 0.13 (Pearson et al., 1995). Conversely, the $^{187}Os/^{188}Os_{(i)}$ ratio from the crust is very high with an average of 1.2 to 1.3 for the upper crust (Esser and Turekian, 1993) and ca. 0.8 for the lower crust (Saal et al., 1998). The initial Os isotope ratio of the molybdenite from the Jinchangyu ores varies narrowly range with a weighted average of 0.015 ± 0.028. It shows initial $^{187}Os/^{188}Os$ ratios closer to those from a mantle reservoir and mantle magmatism lead mineralization initially (Fig. 8).

7.2. The possible relationship between albite and gold

Alkali metasomatism resulting in K–Na alteration is an important exchange processes in endogenetic deposits (Cathles and Shannon, 2007; Du and Wang, 2009; Zhao et al., 1983). For gold deposits, K-alteration is characterized by the growth of K-feldspar and quartz–sericite (–ankerite–pyrite) (Cepedal et al., 2013; Chen et al., 1987; Zhang et al., 2012), and Na-alteration is commonly associated with the presence of albite (Allibone et al., 2004; Harraz, 2002).

The genetic relationship between Na-alteration and gold mineralization has been previously reported, and it has been proposed that this type of alteration is related to early magmatic activity (Mountain and Williams-Jones, 1996; Read and Meinert, 1986). In North America, albite veins have long been known as prospecting clues for the presence of lode quartz-vein gold deposits (e.g. Gallagher, 1940). Albite veins containing gold are probably related to the interplay of polydeformation, metamorphism, and hydrothermal processes (e.g. Read and Meinert, 1986). Such "multiplex gold-bearing veins" are structurally controlled forming in ductile-brittle fractures and felsic igneous rocks where quartz is formed in micro-cracks in albite and calcite at a late stage in the genesis of these veins (e.g. Mountain and Williams-Jones, 1996). Quartz–albite rocks formed during submarine volcanism have also been shown to be important carriers of mantle-derived gold (e.g. Allibone et al., 2004; Golani et al., 2002).

Albite-bearing gold deposits in China include the hydrothermal Dahegu gold deposit in western Guangdong Province (Zhu, 1995), the Hatu porphyry deposit in the Xinjiang Province (An and Zhu, 2007), the Lujia gold deposit in the Jiaodong Peninsula associated with regional metamorphism (Wang et al., 1998), and the Shuangwang gold deposit in the Shanxi Province interpreted as a cryptoexplosion breccia-type gold deposit with extensive red albitisation associated with hydrothermal activity (Liu et al., 2008; Wang et al., 2012).

Like Jinchangyu, albite in gold deposits has some similar features as follows: (1) albite rocks is composed of albite veins or quartz–albite veins; (2) albite is commonly crystallized prior to or during the main mineralization of gold; (3) albite associated with magmatic water; (4) albite veins are associated with a specific structural fabric; (5) albite forming part of the volcanic–magmatic evolution or metasomatism; and (6) albite appears red or pink color in gold deposits.

Precipitation of gold is dependent on many factors in a hydrothermal system, including changes in temperature, pressure, pH, Cl^- concentration, and H_2S fugacity (e.g. Gammons and Williams-Jones, 1997; Zhu et al., 2011). Gold in solution is common in the $AuCl^{-2}$ complex at temperatures higher than 400 °C (Gammons and Williams-Jones, 1997), and in the $Au(HS)^{-2}$ complex at lower temperatures. At these lower temperatures, gold is most soluble around the H_2S–HS^-–SO_4^{2-} equilibrium point and the Au–S complex breaks down with a decline in oxygen fugacity resulting in gold precipitation (Robb, 2009). Studies of fluid inclusions at Jinchangyu have shown that gold-bearing quartz–albite veins form at ~310 °C, suggesting that gold is transported as a $Au(HS)^{-2}$ complex in unsaturated sulfur-bearing fluids. It has been shown earlier that the red veins at Jinchangyu are quartz–albite veins with more hematite than the pink veins. Native gold is commonly precipitate with a reduction in the hematite content and increase in the pyrite content, indicative of changes in redox fronts.

Gold-bearing fluids derived from an alkaline magma are commonly associated with K- and Na-alteration and carbonation. These types of alteration are widely dispersed at Jinchangyu and other gold deposits in the NCC and are considered important prospecting tools for gold exploration (Nie et al., 1994). Consequently, Nie et al. (1994) suggested that a great deal of attention should be paid to the study of alkaline rocks and ore-forming theory related to alteration in the northern margin of the NCC.

Pei and Mei (2003) and Du and Wang (2009) observe that complex anions of ore-forming elements can undergo large-scale migrations in hot fluids that are rich in K^+ or Na^+, and once K^+ and Na^+ are replaced by H^+ (acidification), the complex anions become unstable with hydrolysis and lead to the precipitation of the gold. SiO_2 has its maximum solubility in alkaline solutions rich in K^+ and Na^+, so it can migrate along with the gold (Feng et al., 2013). Furthermore, gold is easily dissolved and migrates in high-temperature fluids in strongly acid or strongly alkaline, oxidizing conditions, and it is easily precipitated in relatively neutral or reducing environments (Chen and Wang, 2004; Zhao and Zhang, 1988; Zhu et al., 2011). The Jinchangyu red quartz–albite veins represent a strongly oxidizing and alkaline environment rich in K^+, Na^+, Ca^{2+}, Mg^{2+}, and Cl^{2-}. It is thus concluded that albite can be an important mineral for the transition between migration and precipitation of the gold in examples such as the Jinchangyu Au deposit.

Table 5
The $\delta^{34}S$ values of ore and rocks from the Jinchangyu Au–Mo deposit.

Sample no.	Comments on host rocks	Analyzed mineral	$\delta^{34}S_{V\text{-}CDT}$‰	Sampling position	
JK321-2	Red quartz–albite vein	Pyrite	0.8	V veins, 63 level, 19 line	This study
JK310-5	Red quartz–albite vein	Pyrite	−3.1	V veins, 103 level, 41 line	This study
JK310-6	Red quartz–albite vein	Pyrite	−1.9	V veins, 103 level, 41 line	This study
JK310-8	Red quartz–albite vein	Pyrite	−2	V veins, 103 level, 41 line	This study
JK301-3	Red quartz–albite vein	Pyrite	−4.1	V veins, −417 level, 7 line	This study
JK301-13	Red quartz–albite vein	Pyrite	−0.2	V veins, −417 level, 7 line	This study
JK306-5	Red quartz–albite vein	Pyrite	−3.2	V veins, −417 level, 31 line	This study
JK309-7	Pink quartz–albite vein	Pyrite	−1.9	V veins, 103 level, 43 line	This study
JK309-8	Pink quartz–albite vein	Pyrite	−2.3	V veins, 103 level, 43 line	This study
JK311-3	Pink quartz–albite vein	Pyrite	−0.1	V veins, 103 level, 37 line	This study
JK311-6	Pink quartz–albite vein	Pyrite	0	V veins, 103 level, 37 line	This study
JK311-7	Pink quartz–albite vein	Pyrite	−0.2	V veins, 103 level, 37 line	This study
JK311-10	Pink quartz–albite vein	Pyrite	−1.1	V veins, 103 level, 37 line	This study
JK311-8	Pink quartz–albite vein	Pyrite	0.1	V veins, 103 level, 37 line	This study
JK313-4	Pink quartz–albite vein	Pyrite	0.4	V veins, 103 level, 31 line	This study
JK311-5	Pink quartz–albite vein	Pyrite	1.5	V veins, 103 level, 37 line	This study
JK316-2	Pink quartz–albite vein	Pyrite	−0.4	V veins, 63 level, 45 line	This study
JK316-7	Pink quartz–albite vein	Pyrite	−2.5	V veins, 63 level, 45 line	This study
JK315-2	Pink quartz–albite vein	Pyrite	0.7	V veins, 63 level, 41 line	This study
JK318-3	Pink quartz–albite vein	Pyrite	−2.3	V veins, 63 level, 37 line	This study
JK319-8	Pink quartz–albite vein	Pyrite	−0.9	V veins, 63 level, 31 line	This study
JK321-5	Pink quartz–albite vein	Pyrite	−1.4	V veins, 63 level, 19 line	This study
JK320-3	Pink quartz–albite vein	Pyrite	0.6	V veins, 63 level, 21 line	This study
JK322-5	Pink quartz–albite vein	Pyrite	−0.1	V veins, 63 level	This study
JK63-37-4	Pink quartz–albite vein	Pyrite	−4.1	III veins, 63 level, 37 line	This study
JK325-1	Pink quartz–albite vein	Pyrite	0.2	V veins, −257 level, 0 line	This study
JK326-4	Pink quartz–albite vein	Pyrite	−3	V veins, −257 level, 11 line	This study
J257-23	Pink quartz–albite vein	Molybdenite	−0.4	III veins, −257 level, 37 line	This study
J417-19	Pink quartz–albite vein	Molybdenite	1.8	III veins, −417 level, 19 line	This study
J23-11	Pink quartz–albite vein	Molybdenite	−2	IV veins, 23 level, 17 line	This study
J23-12	Pink quartz–albite vein	Molybdenite	−2.3	IV veins, 23 level, 17 line	This study
JM-6	Pink quartz–albite vein	Molybdenite	−2.3	V veins, 23 level, 31 line	This study
JK322-7	Quartz vein	Pyrite	−3.6	V veins, 63 level, 1 line	This study
JK322-6	Quartz vein	Pyrite	−1.5	V veins, 63 level, 1 line	This study
JK320-6	Quartz vein	Pyrite	0	V veins, 63 level, 21 line	This study
JK312-4	Quartz vein	Pyrite	−1	V veins, 103 level, 31 line	This study
JK103-37-H1	Quartz vein	Pyrite	1	III veins, 103 level, 37 line	This study
JK17-23-H1	Quartz vein	Pyrite	−4.4	II veins, −17 level, 23 line	This study
JK17-23-5	Quartz vein	Pyrite	−3.9	II veins, −17 level, 23 line	This study
JK323-5	Quartz vein	Pyrite	5	V veins, −257 level, 12 line	This study
JK324-11	Quartz vein	Pyrite	1.9	V veins, −257 level, 8 line	This study
JK305-8	Quartz vein	Pyrite	0.2	V veins, −417 level, 35 line	This study
JK304-1	Quartz vein	Pyrite	0.6	V veins, −417 level, 39 line	This study
7816	Wall rock	Pyrite	3.2	Jinchangyu	Pei and Mei (2003)
7822	Wall rock	Pyrite	1.9	Heishiyu	
7075	Wall rock	Pyrite	2.9	Shibapan	
7901	Wall rock	Pyrite	5.2	Linzigou	
7903	Wall rock	Pyrite	3.6	Jinchangyu	
7904	Wall rock	Pyrite	−1.2	Jinchangyu	
7905	Wall rock	Pyrite	1.3	Linzigou	
103-15	Wall rock	Pyrite	2	103 Level,15 line	Zhang et al. (1991)
223-3-2	Wall rock	Pyrite	2.9	223 Level, 3 line	
IIIP-28	Wall rock	Pyrite	0.8	Heishiyu	
J51-3	Wall rock	Pyrite	0.8	Jinchangyu	Yu and Jia (1989)
J65-2	Wall rock	Pyrite	1.4	Jinchangyu	
J65-7	Wall rock	Pyrite	1.8	Jinchangyu	

7.3. Timing of mineralization at Jinchangyu

The timing of the gold deposits at Jinchangyu is a controversial issue. Compared with the indirect methods used to date the mineralization in the past (Table 6), the Re–Os isotopic dating of molybdenite is not only a direct dating method for sulfides, but also provides a high precision. Fortunately, the presence of molybdenite in the gold-bearing veins at Jinchangyu is available for Re–Os isotopic dating. In addition, the molybdenite and the gold-bearing pyrite have an obvious paragenetic relationship observed in the field. Therefore, the molybdenite age can be used to date the associated gold mineralization at Jinchangyu. The Re–Os dating of molybdenite from Jinchangyu in this study gives a weighted mean age of 225 ± 4 Ma, which is the same within error as the Re–Os isochron date of 223 ± 5 Ma. This date indicates that the Au mineralization at the deposit took place in the Late Triassic.

Most of the gold deposits in eastern Hebei Province are located within 0–5 km of granitic plutons, illustrating that there is an important spatial and probable genetic relationship between Mesozoic granites and gold deposits in the Province (Fig. 1). Studies on the veins, stable isotopes, and fluid inclusions of Jinchangyu gold deposit indicate that the mineralization is associated with deep magmatic activity (Lin and Guo, 1985; Song et al., 2011; Yu and Jia, 1989). This is in accordance with the aeromagnetic surveys which indicate that there has magmatic rock under the gold deposits. The Qingshankou Granite and some other the adjacent plutons form a multiphase body at depth. These buried intrusions show circular structures in Jinchangyu area (Cai et al., 1994;

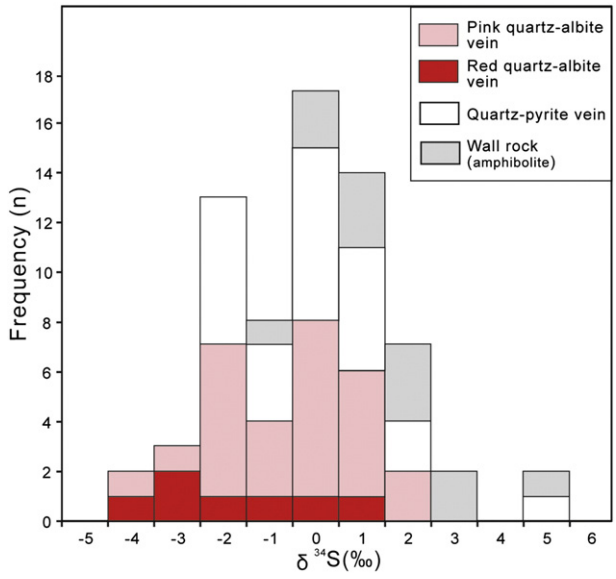

Fig. 12. Histogram of sulfur isotopic compositions of the Jinchangyu Au–Mo deposit.

Xing, 1993), and they may indicate the presence of Triassic-aged intrusions at depth. Song et al. (2013) documented magmatic activities in eastern Hebei Province ranging from 242 Ma to 167 Ma at intervals of around 20 Ma. Li et al. (2002) also report ca. 219–212 Ma gold deposits in the eastern Hebei Province (Table 6). Although these deposits reported by Li et al. (2002) are very small, the date of ca. 225 Ma reported in this study from the significantly larger Jinchangyu Au deposit now extends this age range to ca. 225–212 Ma in the eastern Hebei Province.

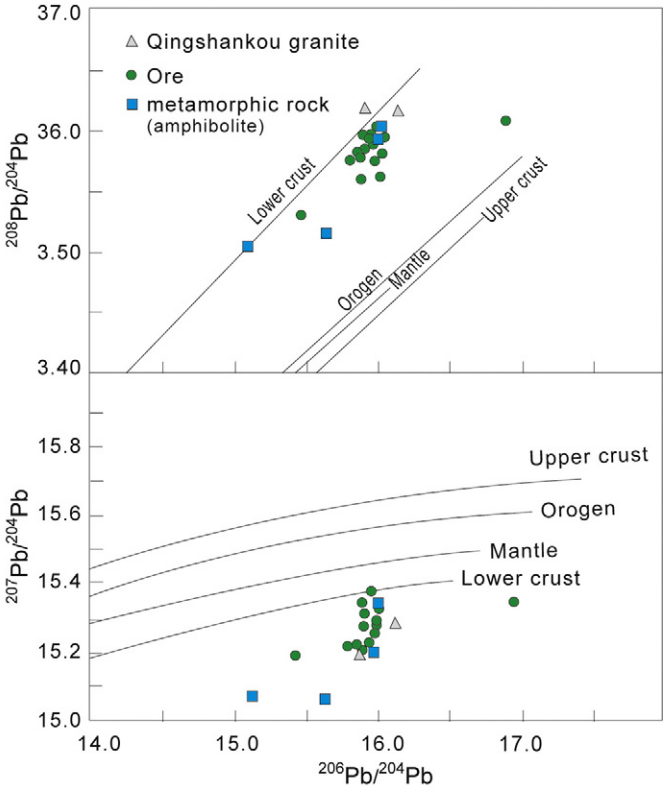

Fig. 13. Lead isotope plots for the Jinchangyu Au–Mo deposit. The evolution lines for major geological units are from Zartman and Haines (1988). Lead isotope data are from Lin and Guo, 1985.

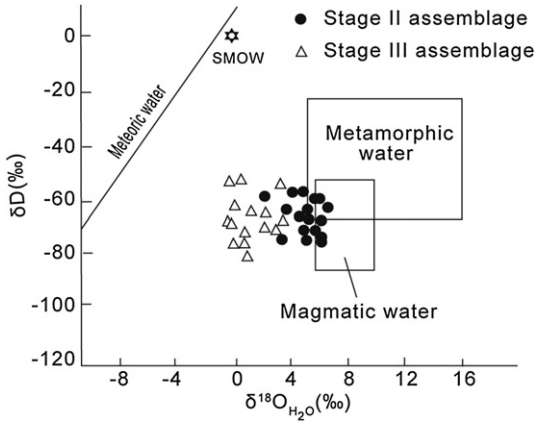

Fig. 14. δD–$\delta^{18}O$ fluid diagram of the Jinchangyu Au–Mo deposit. Base map is cited from Taylor (1997).

The Au mineralization at Jinchangyu is now known to be broadly synchronous with the ca. 223 Ma Dushan Granite and ca. 222 Ma Sanjia Granite (Table 6), indicative of the presence of a significant magmatism during ca. 225 Ma in the region. This synchronicity of significant Au mineralization and magmatism during the mid-Triassic is reason for the further investigation of mid-Triassic granites and their aureoles for the presence of undiscovered Au mineralization.

7.4. Tectonic setting of the Jinchangyu gold deposit

Mesozoic gold occurrences along the northern edge of the NCC are considered to have a complex and poorly understood temporal distribution (Goldfarb et al., 2001), and six episodic mineralizing events may have taken place in the region between 352 and 129 Ma (Hart et al., 2002). Nie et al. (2011) discuss the tectonic setting, timing of ore formation, and metallogenic mechanism of 19 Mo deposits and 4 Au deposits and their relationship with Triassic intrusives located along the northern margin of the craton (Fig. 1a).

This new date of ca. 225 Ma for the Jinchangyu Au deposit, combined with the ca. 212–219 Ma Shuiquangou, Toudaomengou, and Dongzigou deposits in the region (Li et al., 2002), the Jiapigou goldfield in Jilin Province north of Korea (Miao et al., 2005), and the ca. 239 Ma Qingchengzi gold–silver–polymetallic deposits in the Liaoning Province east of Beijing and west of Korea (Xue et al., 2003), indicates that there is a potential gold metallogenic belt along the northern margin of NCC.

The margin of NCC contains the most important gold resources in China. The Xiaoqinling gold metallogenic belt is located on the southern margin (Goldfarb et al., 2014; Mao et al., 2002) and the Jiaodong gold metallogenic belt on the eastern margin (Goldfarb et al., 2014; Mao et al., 2008; Yang and Santosh, 2015). The tectonic setting of these gold metallogenic belts may be related to the destruction of the NCC (Li and Santosh, 2014; Li et al., 2012) or the continental collision between the NCC and Siberian Plate to the north (Chen, 2013; Yang and Santosh, 2015; Zhou et al., 2014). Gold deposits cluster in several regions within the northern margin of the NCC (Hart et al., 2002; Miller et al., 1998; Nie, 1997), and the tectonic setting of these gold deposits is complex, reflecting both Paleo-Asian ocean and younger Pacific margin subduction processes (Goldfarb et al., 2014), in addition to tectonic processes that took place during the Precambrian.

Geochronological, petrological, and structural studies show that the convergence between the Siberian Plate and NCC took place between the late Permian and the Middle Triassic (Chen et al., 2009; Xiao et al., 2009), and the closure of the Paleo-Asian Ocean between these blocks may have taken place at ca. 230 Ma followed by post-orogenic extension (Chen et al., 2009; Jian et al., 2010; Jiang et al., 2012). More Triassic Au deposits have been discovered in this region in recent years, with deposits dating between 245 and 222 Ma, which can be divided into 239

Table 6
Geochronological results of some Au deposits and related granites in the Jinchangyu Au–Mo and its adjacent region.

Sampling location	Geological features	Samples analyzed	Age (Ma)	Analytical method	Reference
Jinchangyu Au deposit	Quartz veins	Zircon	2539 ± 23	U–Pb isotope dilution	Li et al. (2002)
Jinchangyu Au deposit	Quartz–albite vein	Whole rock	2391	Pb–Pb	Zhang et al. (1991)
Jinchangyu Au deposit	Deformed quartz veins	Quartz	2190.5 ± 58	Ar–Ar	Lin et al. (1994)
Jinchangyu Au deposit	Quartz–albite vein	Zircon	1895 ± 2	Zircon SHRIMP U–Pb	Luo et al. (2001)
Jinchangyu Au deposit	Quartz–albite vein	Molybdenite	222.8 ± 4.9	Re–Os isochron	This study
Jinchangyu Au deposit	Sericite schist	Whole rock	197.1	K–Ar	Lin et al. (1994)
Jinchangyu Au deposit	Sericite schist	Sericite	169.8	K–Ar	Yu and Jia (1989)
Jinchangyu Au deposit	Sericite schist	Whole rock	133	Pb–Pb	Yu and Jia (1989)
Yuerya Au deposit	Quartz veins	Molybdenite	168.4 ± 2.7	Re–Os weighted	Song et al. (2013)
Dongzigou Ag-Au deposit	Quartz veins	Quartz	215.3 ± 0.9	Ar–A0072	Li et al. (2002)
Shuiquangou Au deposit	Quartz veins	Quartz	212.5 ± 0.4	Ar–Ar	Li et al. (2002)
Toudaomengou Au deposit	Quartz veins	Quartz	217.3 ± 2.0	Ar–Ar	Li et al. (2002)
Niuxinshan intrusive	Granite	Zircon	173 ± 2	Zircon SHRIMP U–Pb	Guo et al. (2009)
Niuxinshan intrusive	Granite	Zircon	172 ± 2	Zircon SHRIMP U–Pb	Luo et al. (2001)
Yuerya intrusive	Granite	Zircon	174 ± 3	Zircon SHRIMP U–Pb	Luo et al. (2001)
Tangzhangzi intrusive	Granite porphyry	Zircon	173 ± 2	Zircon SHRIMP U–Pb	Guo et al. (2009)
Xiaoyinzi intrusive	Granite	Whole rock	179.5 ± 19	Rb–Sr	Li et al. (2002)
Qinshankou intrusive	Granite	Zircon	199 ± 2	Zircon SHRIMP U–Pb	Luo et al. (2001)
Qinshankou intrusive	Biotite granodiorite	Whole rock	195.6	K–Ar	Lin et al. (1994)
Dushan intrusive	Granite	Zircon	223 ± 2	Zircon SHRIMP U–Pb	Luo et al. (2003)
Dushan intrusive	Granite	Whole rock	248 ± 41	Rb–Sr	Zhang et al. (1991)
Dushan intrusive	Granite	Whole rock	239.1	Ar–Ar	Zhang et al. (1991)
Sanjia intrusive	Granite porphyry	Zircon	222 ± 4	Zircon SHRIMP U–Pb	Luo et al. (2003)

and 245 Ma and 230 and 220 Ma stages (Li and Santosh, 2014; Nie et al., 2011; Zeng et al., 2009). The younger 230–220 Ma stage of mineralization is considered to be related to the closure of the Paleo-Asian Ocean and post-collisional lithospheric extension (Jiang et al., 2014; Meng et al., 2014; Nie et al., 2011; Zhang et al., 2014).

Sillitoe (2002) considers that many Au and Cu–Au rich porphyry deposits are associated with alkaline magmatism under extensional environments in the interiors and along the margins of plates. In this study, we have shown that the Jinchangyu Au deposit, formed at ca. 225 Ma, corresponds to a newly recognized mid-Triassic belt of mineralization along the northern margin of the NCC. This is parallel to the Solonker Suture, which is a major paleo-plate boundary in Asia that stretches northeastwards over 2000 km in Mongolia and China. Consequently, we believe that the Jinchangyu Au deposit can be attributed to the far-field stresses during the continent–continent collision of northern China and Siberian Plate along the northern margin of the NCC in the early Mesozoic (Fig. 15). Gold and molybdenite mineralization occurred across the NCC Paleozoic continental-accretion coeval with emplacement of Triassic felsic or mafic intrusions and exhumation of Precambrian metamorphic rocks. Tectonic reactivation of the cratonic margin and gold deposition coupled with magmatism related to asthenospheric melting triggered by lithosphere delamination.

8. Conclusions

The Jinchangyu Au deposit is structurally controlled in folds and shear zones. The mineralization can be divided into four vein sets which, based on cross-cutting relationship, are grouped as: quartz–albite–hematite veins (Stage I), quartz–albite–polymetallic sulfides veins (Stage II), quartz–pyrite veins (Stage III), and quartz–carbonate veins (Stage IV), with gold being mainly hosted by the Stage II veins.

The albite and hematite alteration at Jinchangyu was produced in a strongly oxidizing and alkaline environment, which was favorable for gold migration in the fluid. The ore forming fluid was rich in H_2O–CO_2

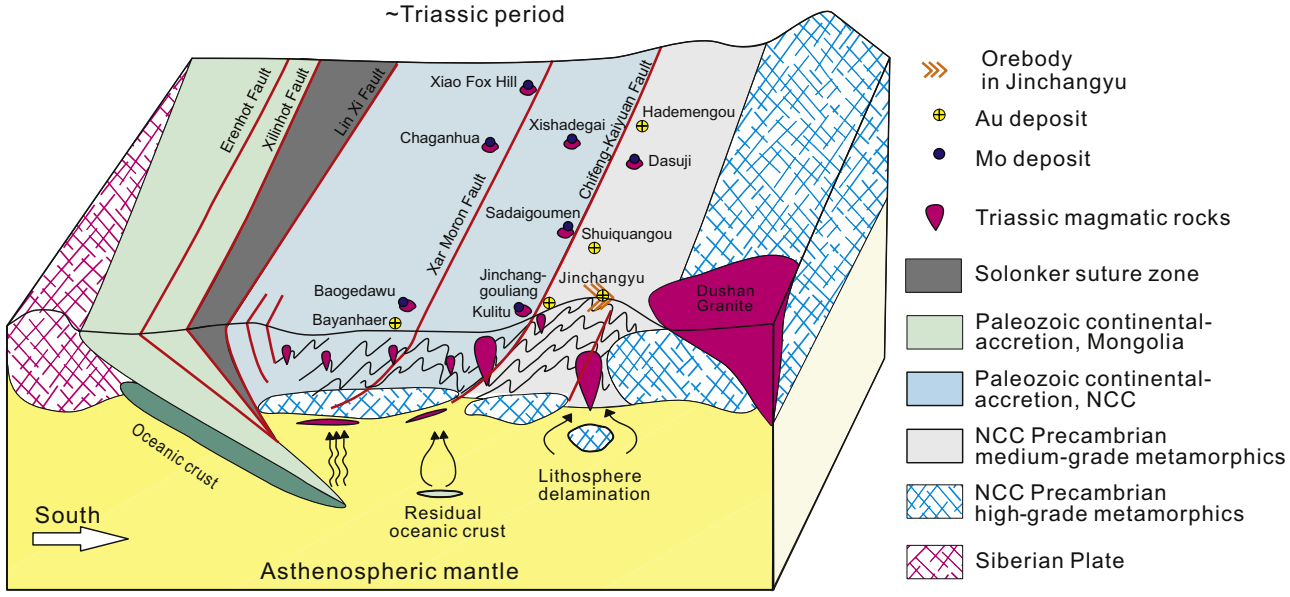

Fig. 15. Tectonic–metallogenic model for the Au–Mo ore belt along the northern margin of the North China Craton.

at moderate temperatures (270°–350 °C) and low to moderate salinities (<13 wt.%). The fluid had a magmatic source during the main stage of mineralization but gradually became meteoric in origin.

The molybdenite Re–Os model ages of 233 to 219 Ma, the weighted mean age of 225 ± 4 Ma, and the isochron age of 223 ± 5 Ma indicate that Au mineralization is Mid-Triassic in age. This is synchronous with the ages of a cluster of gold deposits constituting a metallogenic belt that extends through Hebei, Liaoning into Jilin provinces in China. Finally, the Jinchangyu Au deposit is attributed to the remote far field effect of the final collision between the NCC and Siberian Plate. The native gold and molybdenite mineralization imply an extensional tectonic setting, with the potential for new discoveries at depth.

Acknowledgment

We are grateful to Chief Geologist Yunchen Guo from the Jinchangyu Mining Corporation of Hebei Province for his assistance in field-work. The National Special Research Fund of Chinese Central Government for Basic Scientific Research Operations in Commonweal Research Institutes (No. K1306) and the National Natural Science Foundation of China (No. 41030421 and No. 41273061) helped to sponsor this research. We also acknowledge the Australian Research Council (ARC) Linkage Project LP110100667 and the ARC Centre of Excellence for Core to Crust Fluid Systems (CCFS). This is contribution 451 from CCFS (www.ccfs.mq.edu.au). Drs. Peter C Lightfoot, Xue-Ming Yang and John Ayer are thanked for comments on the manuscript, which helped in improving our article.

References

Allibone, A., Hayden, P., Cameron, G., Duku, F., 2004. Paleoproterozoic gold deposits hosted by albite- and carbonate-altered tonalite in the Chirano District, Ghana, West Africa. Econ. Geol. 99 (3), 479–497.

An, F., Zhu, Y.F., 2007. Studies on geology and geochemistry of alteration-type ore in Hatu gold deposit (western Junggar), Xinjiang, NW China. Mineral Deposits 26 (6), 621–633 (in Chinese with English abstract).

Cai, X.P., Liu, B.G., Ji, Z.L., Qi, X.Y., 1994. Ore-controlling structure and geophysical verification in Jinchangyu gold deposit. Gold Sci. Technol. 2 (5), 1–7 (in Chinese).

Cathles, L.M., Shannon, R., 2007. How potassium silicate alteration suggests the formation of porphyry ore deposits begins with the nearly explosive but barren expulsion of large volumes of magmatic water. Earth Planet. Sci. Lett. 262 (1–2), 92–108.

Cepedal, A., Fuertes-Fuente, M., Martín-Izard, A., García-Nieto, J., Boiron, M.C., 2013. An intrusion-related gold deposit (IRGD) in the NW of Spain, the Linares deposit: Igneous rocks, veins and related alterations, ore features and fluids involved. J. Geochem. Explor. 124, 101–126.

Chen, A.G., 1998. Geometric and kinematic evolution of basement-cored structures: intraplate orogenesis within the Yanshan orogen, northern China. Tectonophysics 292 (1), 17–42.

Chen, Y.J., 2013. The development of continental collision metallogeny and its application. Acta Petrol. Sin. 29, 1–17 (in Chinese with English abstract).

Chen, J., Wang, H.N., 2004. Geochemistry. Science Press (1–418 pp. (in Chinese)).

Chen, G.Y., Sun, D.S., Yin, H.A., 1987. Genetic Mineralogy and Prospecting Mineralogy. Chongqing Publishing House, Chongqin (1–874 pp. (in Chinese with English abstract)).

Chen, B., Jahn, B.M., Tian, W., 2009. Evolution of the Solonker suture zone: constraints from zircon U–Pb ages, Hf isotopic ratios and whole-rock Nd–Sr isotope compositions of subduction- and collision-related magmas and forearc sediments. J. Asian Earth Sci. 34 (3), 245–257.

Clayton, R.N., O'Neil, J.R., Mayeda, T.K., 1972. Oxygen isotope exchange between quartz and water. J. Geophys. Res. 77 (17), 3057–3067.

Du, L.T., Wang, W.G., 2009. Alkaline mantle fluids and alkali-rich hydrothermal metallogenesis. Mineral Deposits 28 (5), 599–610 (in Chinese with English abstract).

Du, A., Wu, S., Sun, D., Wang, S., Qu, W., Markey, R., Stein, H., Morgan, J., Malinovsky, D., 2004. Preparation and certification of Re–Os dating reference materials: molybdenite HLP and JDC. Geostand. Geoanal. Res. 28, 41–52.

Esser, B.K., Turekian, K.K., 1993. The osmium isotopic composition of the continental crust. Geochim. Cosmochim. Acta 57 (13), 3093–3104.

Fan, H.R., Zhai, M.G., Xie, Y.H., Yang, J.H., 2003. Ore-forming fluids associated with granite-hosted gold mineralization at the Sanshandao deposit, Jiaodong gold province, China. Mineral. Deposita 38 (6), 739–750.

Feng, D., Provis, J.L., van Deventer, J.S., 2013. Adsorption of gold on albite in acidic chloride media. Hydrometallurgy 134, 32–39.

Gallagher, D., 1940. Albite and gold. Econ. Geol. 35 (6), 698–736.

Gammons, C.H., Williams-Jones, A.E., 1997. Chemical mobility of gold in the porphyry-epithermal environment. Econ. Geol. 92 (1), 45–59.

Gebre-Mariam, M., Hagemann, S.G., Groves, D.I., 1995. A classification scheme for epigenetic Archaean lode-gold deposits. Mineral. Deposita 30 (5), 408–410.

Golani, P.R., Pandit, M.K., Sial, A.N., Fallick, A.E., Ferreira, V.P., Roy, A.B., 2002. B-Na rich Palaeoproterozoic Aravalli metasediments of evaporitic association, NW India: a new repository of gold mineralization. Precambrian Res. 116 (3–4), 183–198.

Goldfarb, R.J., Leach, D.L., Pickthorn, W.J., Paterson, C.J., 1988. Origin of lode-gold deposits of the Juneau gold belt, southeastern Alaska. Geology 16 (5), 440–443.

Goldfarb, R.J., Groves, D.I., Gardoll, S., 2001. Orogenic gold and geologic time: a global synthesis. Ore Geol. Rev. 18 (1), 1–75.

Goldfarb, R.J., Taylor, R.D., Collins, G.S., Goryachev, N.A., Orlandini, O.F., 2014. Phanerozoic continental growth and gold metallogeny of Asia. Gondwana Res. 25 (1), 48–102.

Guo, S.F., Tang, Z.L., Luo, Z.H., Zhao, W.H., 2009. Zircon SHRIMP U-Pb dating and geological significance from granite bodies in Tangzhangzi and Niuxinshan, eastern Hebei Province, China. Geological Bulletin of China 28 (10), 1458–1464 (in Chinese with English abstract).

Guo, R., Liu, S., Santosh, M., Liu, Shuwen, Santosh, M., Li, Q., Bai, X., Wang, W., 2013. Geochemistry, zircon U–Pb geochronology and Lu–Hf isotopes of metavolcanics from eastern Hebei reveal Neoarchean subduction tectonics in the North China Craton. Gondwana Res. 24 (2), 664–686.

Harraz, H.Z., 2002. Fluid inclusions in the mesozonal gold deposit at Atud mine, Eastern Desert, Egypt. J. Afr. Earth Sci. 35 (3), 347–363.

Hart, C.J.R., Goldfarb, R.J., Qiu, Y., Snee, L., Miller, L.D., Miller, M.L., 2002. Gold deposits of the northern margin of the North China Craton: multiple late Paleozoic–Mesozoic mineralizing events. Mineral. Deposita 37 (3–4), 326–351.

Hoefs, J., 1997. Stable Isotope Geochemistry. Spring, Germany.

Huang, X., Ziwei, B., DePaolo, D.J., 1986. Sm–Nd isotope study of early Archean rocks, Qianan, Hebei Province, China. Geochim. Cosmochim. Acta 50 (4), 625–631.

Jahn, B.M., Auvray, B., Cornichet, J., Bai, Y.L., Shen, Q.H., Liu, D.Y., 1986. 3.5 Ga old amphibolites from eastern Hebei Province, China: field occurrence, petrography, Sm–Nd isochron age and REE geochemistry. Precambrian Res. 34, 311–346.

Jian, P., Lui, D., Kröner, A., Windley, B.F., Shi, Y., Zhang, W., Zhang, F., Miao, L., Zhang, L., Tomurhuu, D., 2010. Evolution of a Permian intraoceanic arc–trench system in the Solonker suture zone, Central Asian Orogenic Belt, China and Mongolia. Lithos 118 (1), 169–190.

Jiang, S.H., Liang, Q.L., Liu, Y.F., Liu, Y., 2012. Zircon U–Pb ages of the magmatic rocks occurring in and around the Dajing Cu–Ag–Sn polymetallic deposit of Inner Mongolia and constrains to the ore-forming age. Acta Petrol. Sin. 28, 495–513 (in Chinese with English abstract).

Jiang, S.H., Liang, Q.L., Bagas, L., 2014. Re–Os ages for molybdenum mineralization in the Fengning region of northern Hebei Province, China: new constraints on the timing of mineralization and geodynamic setting. J. Asian Earth Sci. 79, 873–883.

Kolb, J., Meyer, M.F., 2002. Fluid inclusion record of the hypozonal orogenic Renco gold deposit (Zimbabwe) during the retrograde P-T evolution. Contrib. Mineral. Petrol. 143 (4), 495–509.

Li, S.R., Santosh, M., 2014. Metallogeny and craton destruction: records from the North China Craton. Ore Geol. Rev. 56, 376–414.

Li, J.J., Shen, B.F., Luo, H., Zhai, A.M., Cao, X.L., 2002. Metallogenic epoch of gold deposit in middle north margin of North China Platform. Prog. Precambrian Res. 25 (3), 233–239 (in Chinese with English abstract).

Li, J.W., Bi, S.J., Selby, D., Chen, L., Vasconcelos, P., Thiede, D., Zhou, M.F., Zhao, X.F., Li, Z.K., Qiu, H.N., 2012. Giant Mesozoic gold provinces related to the destruction of the North China craton. Earth Planet. Sci. Lett. 349, 26–37.

Lin, E.W., Guo, Y.J., 1985. Lead isotope studies on goldfields in eastern, Hebei, China. J. Jilin Univ. (Earth Sci. Ed.) 1 (04), 1–10 (in Chinese with English abstract).

Lin, C.Y., He, Y.N., Chen, X.D., Shi, L.B., Zhang, X.O., Qi, X.Y., Hao, R., Gong, R.X., Zhang, J.L., 1994. Relationship between ductile shear zone and gold mineralization — taking Jinchangyu gold mine, eastern Hebei Province, China. Sci. Sin. Chim. 24 (11), 1223–1233.

Liu, S.W., Wang, T., Zeng, R., Xue, C.J., Tang, Y.Z., 2008. Geology and geochemistry of Silurian hydrothermal sedimentary albitite in the Xunyang Basin, southern Qinling. Geol. Explor. 44 (3), 40–46 (in Chinese with English abstract).

Luo, Z.K., Guan, K., Qiu, Y.S., Miao, L.C., Qiu, Y.M., McNaughton, N.J., Groves, D.I., 2001. Zircon SHRIMP U–Pb dating of albite dyke in Jinchangyu gold mine, Jidong area, Hebei, China. Contrib. Mineral. Petrol. 16 (4), 226–231 (in Chinese with English abstract).

Luo, Z.K., Miao, L.C., Guan, K., Qiu, Y.S., Qiu, Y.M., McNaughton, N.J., Groves, D.I., 2003. SHRIMP U- Pb zircon dating of the Dushan granitic batholith and related granite- porphyry dyke, eastern Hebei Province, China, and their geological significance. GEOCHIMICA 32 (2), 173–180 (in Chinese with English abstract).

Mao, J.W., Goldfarb, R.J., Zhang, Z.W., Xu, W.Y., Qiu, Y.M., Deng, J., 2002. Gold deposits in the Xiaoqinling–Xiong'ershan region, Qinling Mountains, central China. Mineral. Deposita 37 (3–4), 306–325.

Mao, J.W., Wang, Y.T., Li, H.M., Pirajno, F., Zhang, C.Q., Wang, R.T., 2008. The relationship of mantle-derived fluids to gold metallogenesis in the Jiaodong Peninsula:evidence from D-O-C-S isotope systematics. Ore Geol. Rev. 33 (3–4), 361–381.

Mei, Y.X., 1997. The metallogenic characteristics and evolution of gold deposits in the Jidong region, Hebei Province, China. Chinese Academy of Geological Sciences, Beijing (in Chinese with English abstract).

Meng, Q.R., Wei, H.H., Wu, G.L., Duan, L., 2014. Early Mesozoic tectonic settings of the northern North China craton. Tectonophysics 611, 155–166.

Miao, L.C., Qiu, Y.M., Fan, W.M., Zhang, F.Q., Zhai, M.G., 2005. Geology, geochronology, and tectonic setting of the Jiapigou gold deposits, southern Jilin Province, China. Ore Geol. Rev. 26 (1), 137–165.

Miller, L.D., Goldfarb, R.J., Nie, F.J., Hart, C., Miller, M.L., Yang, Y.Q., Liu, Y.Q., 1998. North China gold: a product of multiple orogens. SEG Newsl. 33, 1–12.

Mountain, B.W., Williams-Jones, A.E., 1996. Mass transfer and the path of metasomatic reactions in mesothermal gold deposits; an example from Flambeau Lake, Ontario. Econ. Geol. 91 (2), 302–321.

Nie, F.J., 1997. Type and distribution of gold deposits along the northern margin of the North China Craton, People's Republic of China. Int. Geol. Rev. 39 (2), 151–180.
Nie, F.J., Wu, C.Y., Huang, D.H., Zou, T.R., 1994. On the metallogenetic study and prospecting of gold deposits related to sub-alkaline igneous complexes of the north China platform. Chin. Geol. 2, 22–24 (in Chinese with English abstract).
Nie, F.J., Zhang, K., Fei, L.Y., Hong, J.S., Yong, L., 2011. Indosinian magmatic activity and molybdenum, gold mineralization along the northern margin of North China Craton and adjacent area. J. Jilin Univ. (Earth Sci. Ed.) 41 (6), 1651–1666 (in Chinese with English abstract).
Niu, S.Y., LI, F.Y., Chen, H.S., Sun, A.Q., Wang, B.D., Wang, J.Z., Ma, B.J., 2012. The exploration and prognosis in the depth and the periphery of the Jinchangyu gold deposit in eastern Hebei. Chin. Geol. 39 (4), 999–1006 (in Chinese with English abstract).
Pearson, D.G., Shirey, S.B., Carlson, R.W., Boyd, F.R., Pokhilenko, N.P., Shimizu, N., 1995. Re–Os, Sm–Nd, and Rb–Sr isotope evidence for thick Archaean lithospheric mantle beneath the Siberian craton modified by multistage metasomatism. Geochim. Cosmochim. Acta 59 (5), 959–977.
Pei, R.F., Mei, Y.X., 2003. The evolution of the metallogenic provinces and ore-forming chronology — a case study of the metallogenic province in the northern margin of the North China Platform. Geological Publishing House, Beijing (1-199 pp. (in Chinese with English abstract)).
Pirajno, F., Bagas, L., 2008. A review of Australia's Proterozoic mineral systems and genetic models. Precambrian Res. 166, 54–80.
Read, J.J., Meinert, L.D., 1986. Gold-bearing quartz vein mineralization at the Big Hurrah Mine, Seward Peninsula, Alaska. Econ. Geol. 81 (7), 1760–1774.
Robb, L., 2009. Introduction to Ore-Forming Processes. John Wiley & Sons.
Saal, A.E., Rudnick, R.L., Ravizza, G.E., 1998. Re–Os isotope evidence for the composition, formation and age of the lower continental crust. Nature 393, 58–61.
Schaefer, B.F., 2004. ^{187}Re–^{188}Os isotopes in metallogenesis: an overview. Predictive Mineral Discovery CRC Conference.
Selby, D., Creaser, R.A., 2004. Macroscale NTIMS and microscale LA–MC–ICP–MS Re–Os isotopic analysis of molybdenite: testing spatial restrictions for reliable Re–Os age determinations, and implications for the decoupling of Re and Os within molybdenite. Geochim. Cosmochim. Acta 68, 3897–3908.
Shirey, S.B., Walker, R.J., 1995. Carius tube digestion for low-blank rhenium–osmium analysis. Anal. Chem. 67, 2136–2141.
Sillitoe, R.H., 2002. Some metallogenic features of gold and copper deposits related to alkaline rocks and consequences for exploration. Mineral. Deposita 37 (1), 4–13.
Smoliar, M.I., Walker, R.J., Morgan, J.W., 1996. Re–Os ages of group IIA, IIIB, IVA, IVB iron meteorites. Science 271, 1099–1102.
Song, Y., Wang, R., Hu, J., Tan, Y., Shi, C., Wang, T., 2011. Ore-controlling structure characteristic and the sources of ore forming material in the Jinchangyu gold deposit, Hebei province. Acta Geol. Sin. 85 (1), 78–87 (in Chinese with English abstract).
Song, Y., Wang, S.Z., Hu, J.Z., Nie, F.J., Tan, Y.J., Wang, Z.Y., 2013. Gold mineralization and evolution under structural constraints of the basement in the Jidong Area, North China Craton. Geotecton. Metallog. 37 (3), 410–421 (in Chinese with English abstract).
Stein, H.J., Scherstén, A., Hannah, J., Markey, R., 2003. Subgrain-scale decoupling of Re and 187Os and assessment of laser ablation ICP–MS spot dating in molybdenite. Geochim. Cosmochim. Acta 67, 3673–3686.
Sun, D.Z., 1984. The Early Precambrian Geology of the Eastern Hebei. Tianjin Science and Technology Press, Tianjin (1-273 pp. (in Chinese with English abstract)).
Taylor, H.P., 1997. Oxygen and hydrogen isotope relationships in hydrothermal mineral deposits. In: Barnes, H.L. (Ed.), Geochemistry of Hydrothermal Ore Deposits. Wiley and Sons, New York, pp. 229–302.
Wang, S.Q., 1989. Metallogeny of gold deposits in the North China Platform. J. SE Asian Earth Sci. 3 (1), 351–358.
Wang, R.M., He, S.Y., Chen, Z.Z., Li, P.F., Dai, F.Y., 1985. Geochemical evolution and metamorphic development of the early Precambrian in eastern Hebei, China. Precambrian Res. 27 (1), 111–129.
Wang, Z.M., Chen, G.Y., Shao, W., 1998. Genetic mineralogy of albites in lujia gold deposit. Geoscience 12 (2), 210–213.
Wang, K.X., Wang, J.P., Liu, J.J., Zeng, X.T., Cao, R.R., Hui, D.F., Cheng, J.J., Zhang, J.L., Li, Z.G., Li, X.G., 2012. Geology and stable isotope geochemistry of the Shuangwang gold deposit in Taibai County, Shaanxi Province. Chin. Geol. 39 (5), 1359–1374 (in Chinese with English abstract).
Witt, W.K., Knight, J.T., Mikucki, E.J., 1997. A synmetamorphic lateral fluid flow model for gold mineralization in the Archean southern Kalgoorlie and Norseman terranes, Western Australia. Econ. Geol. 92 (4), 407–437.
Xiao, W.J., Windley, B.F., Huang, B.C., Han, C.M., Yuan, C., Chen, H.L., Sun, M., Sun, S., Li, J.L., 2009. End-Permian to mid-Triassic termination of the accretionary processes of the southern Altaids: implications for the geodynamic evolution, Phanerozoic continental growth, and metallogeny of Central Asia. Int. J. Earth Sci. 98, 1189–1217.
Xing, L.X., 1993. The circular structure and geological meaning study for Jinchangyu area. J. Jilin Univ. (Earth Sci. Ed.) 23 (4), 400–404.
Xue, C.J., Chen, Y.C., Lu, Y.F., Li, H.Q., 2003. Metallogenic epochs of Au and Ag deposits in Qingchengzi ore-clustered area, eastern Liaoning Province. Mineral Deposits 22 (2), 177–184.
Yang, Q.Y., Santosh, M., 2015. Early Cretaceous magma flare-up and its implications on gold mineralization in the Jiaodong Peninsula, China. Ore Geol. Rev. 65 (3), 626–642.
Yu, C.T., Jia, B., 1989. Study on the genesis of major types of gold deposits and its mechanism of formation in eastern Hebei. Geological Publishing House, Beijing, pp. 1–48 (in Chinese with English abstract).
Zartman, R.E., Haines, S.M., 1988. The plumbotectonic model for Pb isotopic systematics among major terrestrial reservoirs—a case for bi-directional transport. Geochim. Cosmochim. Acta 52 (6), 1327–1339.
Zeng, Q.D., Liu, J.M., Zhang, Z.L., Chen, W.J., Qin, F., Zhang, R.B., Yu, W.B., Zhang, X.H., Zhai, M.G., 2009. Mineralizing types, geological characteristics and geodynamic background of molybdenum deposits in Xilamulun molybdenum polymetal metallogenic belt on northern margin of North China Craton. Acta Petrol. Sin. 5, 1225–1238 (in Chinese with English abstract).
Zhang, Q.S., Yang, Z.S., Gao, D.Y., 1991. Jidong Jinchangyu Regional High-Grade Metamorphic Geology and Gold Deposits. Geological Publishing House, Beijing (1-445 pp. (in Chinese)).
Zhang, X.H., Liu, Q., Ma, Y.J., Wang, H., 2005. Geology, fluid inclusions, isotope geochemistry, and geochronology of the Paishanlou shear zone-hosted Gold Deposit, North China Craton. Ore Geol. Rev. 26 (3), 325–348.
Zhang, C.H., Li, C.M., Deng, H.L., Liu, Y., Liu, L., Wei, B., Li, H.B., Liu, Z., 2011. Mesozoic contraction deformation in the Yanshan and northern Taihang mountains and its implications to the destruction of the North China Craton. Sci. China Earth Sci. 54 (6), 798–822 (in Chinese with English abstract).
Zhang, G.R., Xu, J.H., Wei, H., Song, G.C., Zhang, Y.B., Zhao, J.K., He, B., Chen, D.L., 2012. Structure, alteration, and fluid inclusion study on deep and surrounding area of the Dongping gold deposit, northern Hebei, China. Acta Petrol. Sin. 28 (2), 637–651 (in Chinese with English abstract).
Zhang, S.H., Zhao, Y., Davis, G.A., Ye, H., Wu, F., 2014. Temporal and spatial variations of Mesozoic magmatism and deformation in the North China Craton: implications for lithospheric thinning and decratonization. Earth Sci. Rev. 131, 49–87.
Zhao, L.S., Zhang, B.R., 1988. Geochemistry. Geological Publishing House, Beijing (1-404 pp. (in Chinese)).
Zhao, Y.M., Si, B.C., Xin, L.D., 1983. The characteristics of volatile components and alkaline metasomatism in main skarn-type iron deposits of China and their role in ore deposit formation. Geol. Rev. 29 (1), 66–74.
Zhong, H., Zhao, Y.Z., Yan, L., 1996. Gold Mine in East of Jidong Region. Metallurgical Industry Press, Beijing (in Chinese).
Zhou, Z.J., Chen, Y.J., Jiang, S.Y., Zhao, H.X., Qin, Y., Hu, C.J., 2014. Geology, geochemistry and ore genesis of the Wenyu gold deposit, Xiaoqinling gold field, Qinling Orogen, southern margin of North China Craton. Ore Geol. Rev. 59, 1–20.
Zhu, D.G., 1995. The relationship between albitization in ductile shear zone and gold in Dahegu gold deposit in the north of Guangdong province. J. Geomech. 1 (1), 88–95.
Zhu, Y.F., An, F., Tan, J.J., 2011. Geochemistry of hydrothermal gold deposits: a review. Geosci. Front. 2 (3), 367–374.